nature communications

Article

https://doi.org/10.1038/s41467-025-58033-9

Plant essential oil targets TRPV3 for skin renewal and structural mechanism of action

Received: 17 October 2024

Accepted: 5 March 2025

Published online: 19 March 2025

Check for updates

Yang Li[1,5], Xuteng Lu[1,5], Xufeng Cheng[1], Keyu Xia[1], Junyan Hu[1], Peiyu Wang[1], Peiyuan Pang[1], Bomin Gao[1], Demeng Sun[2], Zhuzhen Zhang[1], Dongdong Li[3], Zengqin Deng[4], Changlin Tian[2], Chang Xie[1] & Jing Yao[1]

Our skin safeguards the body homeostasis for health and also provides psychological consolation in social life. Natural essential oils are widely used for skin maintenance, while the molecular target and mechanism of action remain largely unknown. Here, we report that citronellal, a plant-derived acyclic monoterpene commonly used for personal care, stimulates skin renewal by promoting keratinocyte proliferation through the activation of TRPV3. We further present cryo-EM structures of human TRPV3 in complex with acyclic monoterpenes, including citronellal, citral, linalool and isodihydrolavandulal, determined at resolutions of 3.1-3.6 Å. Our structural and functional analysis unmasks consistent yet subtly different binding modes within the TRPV3 vanilloid site. Our results elucidate that essential oil ligands activate TRPV3 channels by competitively displacing endogenous lipids from the vanilloid site. Together, these findings identify TRPV3 as the molecular target of natural acyclic monoterpenes for skin renewal, and delineate the structural basis of action, thus being instrumental for moving forward skin healthcare.

The skin serves as the body's primary barrier, protecting internal tissues from environmental hazards, pathogens, and physical injury. The skin is integrated with the nervous system and is involved in thermoregulation and the perception of physical and chemical stimuli[1]. In addition, the skin is intricately linked with our emotional and social well-being[2]. Maintaining optimal skin condition is therefore beneficial for physical health, psychological comfort, and social interactions. Essential oils, which are derived from aromatic plants, are natural products that have traditionally been used for the skin care and maintenance, as well as in aromatherapy, food flavoring and pharmacological assistance. The main bioactive constituents of plant-derived essential oils are monoterpenes, which encompass acyclic, monocyclic and bicyclic compounds[3]. Acyclic monoterpenes possess antioxidant and analgesic properties, which are beneficial in the context of diabetic cardiomyopathy and atherosclerosis. In addition, they serve to attenuate nociception and anxiety-related symptoms[4]. One of the most prevalent types of monoterpenes is citronellal, which is typically obtained by steam distillation of certain plant species, particularly the *Cymbopogon genus*. It serves as a valuable component of citronella oil and is used in the anti-aging cosmetics[5]. Furthermore, other acyclic monoterpenes, such as citral and linalool, are also used for personal care purposes, such as relieving acne and other skin abnormalities[6]. Despite the long history of plant essential oils in skin care, the molecular target and underlying mechanisms of action remain elusive.

Keratinocyte proliferation represents a pivotal process in skin regeneration, anti-aging interventions, and wound healing. Transient

[1]State Key Laboratory of Virology and Biosafety, TaiKang Center for Life and Medical Sciences, College of Life Sciences, Hubei Key Laboratory of Cell Homeostasis, Frontier Science Center for Immunology and Metabolism, Wuhan University, Wuhan, Hubei, China. [2]Department of Chemistry and the First Affiliated Hospital of USTC, School of Life Sciences, Division of Life Sciences and Medicine, Joint Center for Biological Analytical Chemistry, Anhui Engineering Laboratory of Peptide Drug, Anhui Laboratory of Advanced Photonic Science and Technology, University of Science and Technology of China, Hefei, Anhui, China. [3]Sorbonne Université, CNRS, Inserm, Institut de Biologie Paris Seine (IBPS), Center for Neuroscience at Sorbonne Université (NeuroSU), Paris, France. [4]Key Laboratory of Virology and Biosafe, Wuhan Institute of Virology, Chinese Academy of Sciences, Wuhan, Hubei, China. [5]These authors contributed equally: Yang Li, Xuteng Lu. e-mail: jyao@whu.edu.cn

receptor potential vanilloid 3 (TRPV3) is a calcium-permeable and non-selective cation channel that is abundantly expressed in skin keratinocytes[7–9] and promotes keratinocyte proliferation via an EGFR-dependent signaling pathway[10]. As a polymodal cellular sensor, TRPV3 integrates a broad spectrum of endogenous and exogenous stimuli and plays a role in maintaining the skin barrier formation and thermosensation[11]. Deficiency of TRPV3 has been linked to impaired skin wound healing process and abnormal hair morphogenesis, which is characterized by curly whiskers and wavy hair coats[12–14]. Pharmacological overactivation or genetic gain-of-function mutations of TRPV3 in rodents have been observed to result in a hairless phenotype and pruritic dermatitis[15,16]. Furthermore, hyperactive TRPV3 mutants have been identified in patients diagnosed with Olmsted syndrome[17,18]. Thus, a precisely calibrated level of TRPV3 function is crucial for maintaining the skin health, physiology and renewal.

In the present study, we identify citronellal as a selective agonist of TRPV3 and demonstrate that citronellal promotes skin renewal by enhancing keratinocyte proliferation through TRPV3 activation of a beneficial range. In addition, we present cryo-EM structures of TRPV3-citronellal and other acyclic monoterpene ligand complexes, revealing a general hydrophobic binding pocket. Furthermore, our results indicate that ligand binding results in the expulsion of endogenous lipids from the vanilloid site, which underlies conformational changes in TRPV3 and ultimately leads to pore dilation. Taken together, these findings elucidate the molecular mechanism underlying the beneficial effects of plant monoterpenes on skin health, while advancing our understanding of TRPV3 pharmacology and its adaptation to skin well-being.

Results

Citronellal promotes skin renewal by activating keratinocyte TRPV3

To assess the beneficial effects of acyclic monoterpenes on the skin, we applied a topical solution of 1% citronellal essential oil or a control solution to the depilated dorsal skin of mice for a period of 3 weeks (Fig. 1a), as natural essential oils are typically diluted to 0.2% - 5% for use in skin healthcare[19]. During the study period, no difference in tumor necrosis factor-α (TNF-α) mRNA expression levels was observed between the vehicle and 1% citronellal-treated groups (Supplementary Fig. 1a), thereby excluding the occurrence of local inflammation. In addition, no maladaptive or adverse symptoms were observed in either group, indicating that an appropriate dose of citronellal is safe for topical application to the skin. Since keratinocyte proliferation is a crucial process in skin renewal, we next investigated the effect of citronellal treatment on keratinocyte proliferation. Hematoxylin and eosin (H&E) staining results showed that the topical application of 1% citronellal resulted in a significant increase in epidermal thickness compared to that of the vehicle (Fig. 1b, c). Conversely, there was no significant difference in the dermal thickness between the groups (Fig. 1d), suggesting that citronellal administration did not induce an inflammatory response in the skin. Our results showed a significant increase in keratin14 stratum thickness in the citronellal group compared to the vehicle group (Fig. 1e, f). The enhancement effect of citronellal on skin renewal was observed after two weeks of application, indicating that essential oils in skin care require long-term application to be effective. In contrast, topical application of 1% citronellal had no discernible effect on the keratin10 stratum during the application period (Fig. 1g, h).

To probe the molecular target of citronellal in skin renewal, we isolated primary keratinocytes from neonatal mouse skin. The keratinocytes exhibited predominant expression of keratin14, with minimal expression of keratin10 expression (Supplementary Fig. 1b,c), confirming their proliferative nature. Given the essential function of Ca^{2+} in keratinocyte activity[20], we sought to examine whether citronellal induced calcium influx using fluo-4 AM-based calcium imaging. Indeed, we observed that citronellal induced pronounced Ca^{2+} increases in isolated keratinocytes when exposed to 4 mM citronellal with 1.8 mM extracellular Ca^{2+}, whereas no such response was observed in a calcium-free extracellular solution (Fig. 1i, j). As a positive control, the Ca^{2+} ionophore ionomycin (1 μM) was applied after citronellal application to induce a maximal intracellular Ca^{2+} elevation for comparison[21]. These results suggest that citronellal may function as an agonist to activate a ligand-gated calcium-permeable ion channel, thereby causing an influx of extracellular calcium ions into the cytoplasm. We then carried out the whole-cell voltage clamp recordings in primary keratinocytes and found that citronellal could elicit inward currents at the holding potential of -60 mV in a dose-dependent manner with an EC_{50} of 5.46 ± 0.27 mM and an n_H of 3.92 ± 0.63 ($n = 6$; Fig. 1k,l). Notably, the currents activated by repeated application of citronellal showed a progressive increase (Supplementary Fig. 1d), exhibiting characteristics similar to the sensitization process of TRPV3[22], an ion channel abundantly expressed in keratinocytes[8]. Dyclonine, a selective TRPV3 inhibitor that we identified recently[23], indeed inhibited citronellal-evoked currents in a concentration-dependent manner (IC_{50} = 0.83 ± 0.04 μM, n_H = 3.72 ± 0.48, $n = 5$) (Fig. 1k, l), suggesting that the currents were mediated by TRPV3 channels. We then expressed mouse TRPV3 (mTRPV3) in HEK 293 T cells and performed patch-clamp recordings. As shown in the Supplementary Fig. 1e, citronellal acts as an agonist of the TRPV3 channel (EC_{50} = 5.29 ± 0.17 mM, n_H = 3.79 ± 0.41, $n = 7$) and dyclonine effectively inhibits citronellal-induced TRPV3 currents (IC_{50} = 0.73 ± 0.05 μM, n_H = 3.37 ± 0.58, $n = 7$). In addition, citronellal-evoked currents exhibited outward rectification in epidermal keratinocytes (Supplementary Fig. 1f), similar to the currents recorded in HEK 293 T cells exogenously expressing mTRPV3 (Supplementary Fig. 1g). Notably, the properties of citronellal-evoked TRPV3 channel currents obtained in the exogenous expression system remain consistent with those observed in primary keratinocytes. To further clarify the activating effect of citronellal on TRPV3 channels, we proceeded to separately express several TRP channels in HEK 293T cells, including TRPV1, TRPV2, TRPV4, TRPM8, and TRPA1 channels, which have been previously reported to be expressed in keratinocytes. We then examined the response of these channels to citronellal using whole-cell patch-clamp recordings, which showed that citronellal selectively activated TRPV3 channels without a significant activation effect on other channels (Fig. 1m). Single-channel recordings were obtained from the outside-out membrane patches of TRPV3-expressing HEK 293T cells (Fig. 1n), perfused with citronellal under different voltage clamps ranging from −100 to +100 mV. When comparing the *I–V* curves between citronellal and the activation of a broad-spectrum TRPV agonist 2-APB, a similar shape was observed (Fig. 1o). Together, these results indicate that citronellal stimulates skin regeneration by selectively targeting the TRPV3 channel.

TRPV3 deficiency impairs the effect of citronellal on skin renewal

To substantiate the critical function of the TRPV3 channel in citronellal-facilitated skin regeneration, we utilized *Trpv3*$^{-/-}$ mice to elucidate the functional role of TRPV3 in this process. In contrast to wild-type cells, the calcium imaging results showed that *Trpv3*$^{-/-}$ keratinocytes lost response to citronellal challenge, regardless of the extracellular calcium concentration (Fig. 2a, b). As corroboration, whole-cell recordings in *Trpv3*$^{-/-}$ keratinocytes showed no measurable inward currents when exposed to varying concentrations of citronellal (Fig. 2c, d). In contrast to the wild type (WT) animals, no notable discrepancies in epidermal or dermal thickness, along with keratin14 and keratin10 expression, were observed between the vehicle and citronellal-treated cohorts in *Trpv3*$^{-/-}$ mice (Fig. 2e–h). Because keratinocyte-derived growth factors play a critical role in skin regeneration, we next examined the expression levels of transforming growth factor-α (TGF-α), transforming growth factor-β (TGF-β), vascular endothelial growth factor (VEGF), and tissue inhibitor of metalloproteinase-1 (TIMP1). As illustrated in Fig. 2i–l, results of the

https://doi.org/10.1038/s41467-025-58033-9

qRT-PCR analyses showed that citronellal significantly upregulated the mRNA levels of these growth factors in skin samples treated with 1% citronellal from WT mice, but not from *Trpv3*$^{-/-}$ mice. These results validate that citronellal promotes skin renewal by targeting the TRPV3 channel.

Citronellal promotes proliferation of human keratinocyte line through TRPV3 activation

In view of the above findings indicating that citronellal stimulates keratinocyte proliferation via TRPV3 in mice, we proceeded to investigate the proliferative effects of citronellal on human cells using

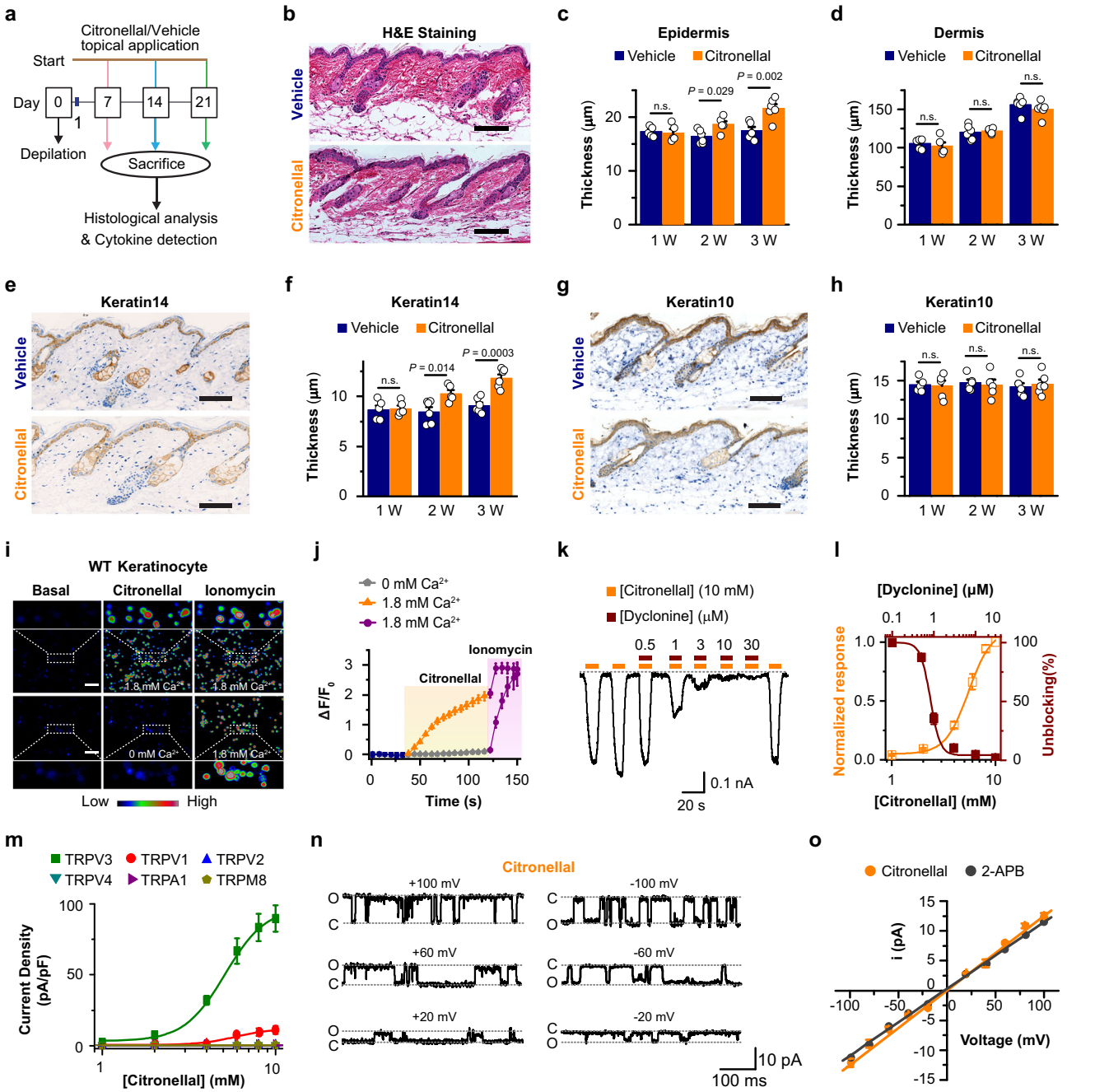

Fig. 1 | Citronellal promotes skin renewal and selectively activates TRPV3. **a** Schematic illustrating the experiments for topical treatment of mouse skin with citronellal. Representative images of H&E staining (**b**), keratin14 (**e**) and keratin10 (**g**) of skin sections obtained from mice treated with vehicle or 1% citronellal for 3 weeks. Scale bars are 100 μm. Summary data for the effects of citronellal on the thickness of the epidermis (**c**), dermis (**d**), keratin14 (**f**) and keratin10 (**h**) in wild-type (WT) mice. $n = 5$ or 6 mice/group. **i** $[Ca^{2+}]_i$ increases induced by different treatments. Scale bar is 60 μm. **j** The relative change of fluorescence was plotted from the images shown in (**i**). $n = 38$ cells for 1.8 mM Ca^{2+} condition, $n = 31$ cells for 0 mM Ca^{2+} condition. **k** The typical response of epidermal keratinocyte to citronellal and dyclonine as indicated. Holding potential was −60 mV. **l** Normalized dose-response curves of citronellal-evoked currents (orange, $n = 6$ cells, $EC_{50} = 5.46 \pm 0.27$ mM and $n_H = 3.92 \pm 0.63$) and dyclonine inhibition of citronellal-evoked currents (wine, $n = 5$ cells, $IC_{50} = 0.83 \pm 0.04$ mM and $n_H = 3.72 \pm 0.48$) in WT keratinocytes. **m** Concentration-response curves of citronellal for activation of HEK 293 T cells that had been exogenously expressed with mTRPV3 (olive, $n = 7$ cells, $EC_{50} = 5.29 \pm 0.17$ mM and $n_H = 3.79 \pm 0.41$), mTRPV1 (red, $n = 6$ cells, $EC_{50} = 5.93 \pm 0.2$ mM and $n_H = 4.04 \pm 0.43$), mTRPV2 (blue, $n = 5$ cells), rTRPV4 (dark cyan, $n = 5$ cells), mTRPA1 (purple, $n = 8$ cells) and rTRPM8 (dark yellow, $n = 6$ cells). **n** Single-channel currents of mTRPV3 evoked by 6 mM citronellal. **o** I–V relationships of TRPV3 single-channel current evoked by 6 mM citronellal (wine, $n = 7$ cells) or 10 μM 2-APB (*blue*, $n = 6$ cells). Two-tailed unpaired t-tests were used for statistical analysis in (**c**), (**d**), (**f**) and (**h**). Data are presented as mean ± SEM; $^*P < 0.05$, $^{**}P < 0.01$, $^{***}P < 0.001$, n.s stands for not significant.

https://doi.org/10.1038/s41467-025-58033-9

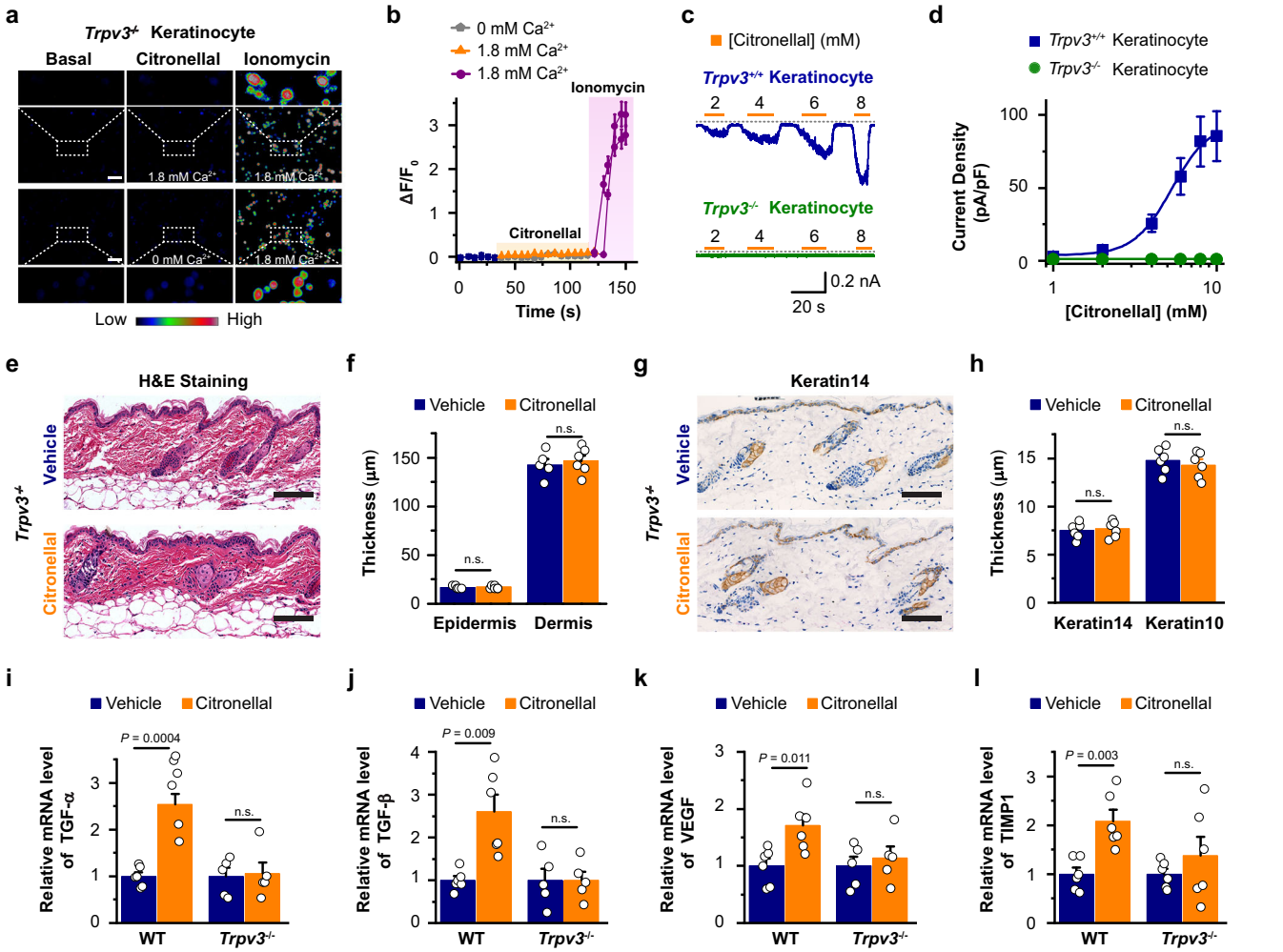

Fig. 2 | TRPV3 deficiency impairs the effect of citronellal on skin renewal. **a** Responses of primary cultured keratinocytes from *Trpv3*$^{-/-}$ mice were consecutively challenged with citronellal and ionomycin in the presence of 1.8 mM Ca^{2+} or free Ca^{2+}, as indicated. Scale bars represent 60 μm. **b** Time courses of the relative change of fluorescence were plotted from the images shown in (**a**). $n = 36$ cells for 1.8 mM Ca^{2+} condition, $n = 37$ cells for 0 mM Ca^{2+} condition. **c** Representative whole-cell recordings from a *Trpv3*$^{+/+}$ keratinocyte and a *Trpv3*$^{-/-}$ keratinocyte showing the responses to varying concentrations of citronellal. Holding potential was −60 mV. The dotted line indicates the zero current level. **d** Dose-response curves of citronellal in *Trpv3*$^{+/+}$ keratinocytes ($n = 6$ cells) and *Trpv3*$^{-/-}$ keratinocytes ($n = 7$ cells). Fitting by Hill's equation yielded an $EC_{50} = 5.46 \pm 0.27$ mM and $n_H = 3.92 \pm 0.63$ for *Trpv3*$^{+/+}$ keratinocytes. **e** Representative images of H&E-stained skin sections obtained from *Trpv3*$^{-/-}$ mice that were topically treated with either citronellal (1%) or vehicle for a period of 3 weeks. Scale bars represent 100 μm. **f** Average plot of the effects of citronellal on epidermal and dermal thickness in *Trpv3*$^{-/-}$ mice. $n = 5$ or 6 mice/group. **g** Representative immunostaining images of keratin14 in skin sections obtained from *Trpv3*$^{-/-}$ mice that were topically treated with 1% citronellal or vehicle for 3 weeks. Scale bars represent 100 μm. **h** Statistical plot of the effects of citronellal on keratin14 and keratin10 in skin sections derived from *Trpv3*$^{-/-}$ mice. $n = 5$ or 6 mice/group. qRT-PCR analysis of TGF-α (**i**), TGF-β (**j**), VEGF (**k**) and TIMP1 gene expression in skin samples obtained from WT and *Trpv3*$^{-/-}$ mice treated with vehicle or 1% citronellal for 3 weeks. $n = 5$ or 6 mice/group. Two-tailed unpaired t-tests were used for statistical analysis in (**f**), (**h**), (**i**), (**j**), (**k**) and (**l**). Data are presented as mean ± SEM; $^*P < 0.05$, $^{**}P < 0.01$, $^{***}P < 0.001$, n.s stands for not significant.

immortalized human keratinocytes (HaCaT). Immunostaining confirmed a high level of TRPV3 protein distribution in HaCaT cells (Fig. 3a). As observed in mouse keratinocytes, citronellal induced a significant increase in intracellular Ca^{2+} levels in HaCaT cells when incubated in a 1.8 mM Ca^{2+} solution, but not in a calcium-free solution (Fig. 3b). Whole-cell recordings demonstrated that citronellal activated the human TRPV3 (hTRPV3) channel in a dose-dependent manner, with $EC_{50} = 5.78 \pm 0.72$ mM, $n_H = 3.76 \pm 1.39$ ($n = 7$) (Fig. 3c). Since TRPV3 is a temperature-sensitive ion channel with a threshold of ~50 °C which however becomes responsive to warm temperatures after intensive stimulation[24]. In addition, temperature has been proven to synergize with other agonists on TRPV3[25]. Hereby, we assessed the efficacy of citronellal in activating TRPV3 at the physiological temperature 37 °C. As the temperature increased, the effect of citronellal on hTRPV3 activation became markedly more pronounced. The EC_{50} of citronellal on hTRPV3 activation was observed to shift from 5.77 ± 0.51 mM to 1.31 ± 0.04 mM when the temperature was increased from 23 °C to 37 °C (Fig. 3d). We then evaluated the effect of citronellal on cell viability using a calcein fluorescence assay (Supplementary Fig. 2). Incubation of HaCaT cells with citronellal concentrations of 0.1, 0.2, and 0.5 mM at 37 °C did not result in a statistically significant alteration in cell viability compared to the vehicle control. However, citronellal showed a potential decline in cell viability at a higher concentration of 1 mM at 37 °C (Fig. 3e). We also performed Edu cell proliferation assays at 37 °C and observed that citronellal facilitated HaCaT cell proliferation within a certain concentration range (0.2–0.5 mM), but inhibited proliferation at concentrations exceeding 1 mM (Fig. 3f, g). Hence, application of a modest concentration of citronellal is necessitated for beneficial effects.

Furthermore, the blockade of the TRPV3 channel by dyclonine (10 μM) was also found to effectively suppress citronellal-induced proliferation of HaCaT cells (Fig. 3h). Given the substantial influx of

https://doi.org/10.1038/s41467-025-58033-9

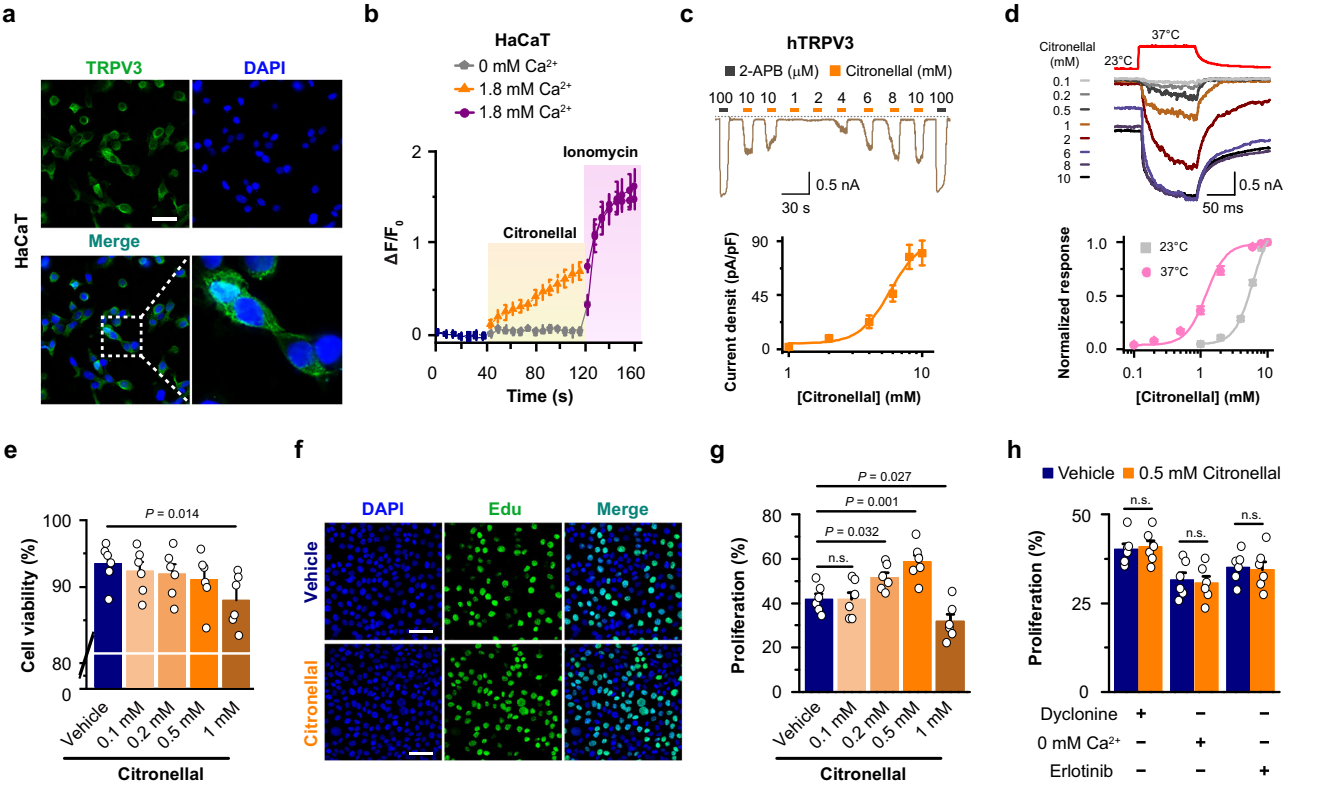

Fig. 3 | Citronellal promotes keratinocyte proliferation via TRPV3 channel-induced Ca^{2+} influx and EGFR signaling pathway. a Representative immunostaining images of TRPV3 in HaCaT cells. Nuclei are marked by DAPI. The enlarged image indicates HaCaT cells express a certain level of TRPV3. Scale bar is 30 μm. **b** Time courses of the relative change of fluorescence in HaCaT cells challenged with citronellal or ionomycin in the presence of 1.8 mM Ca^{2+} ($n = 35$ cells) and free Ca^{2+} ($n = 31$ cells) as indicated. **c** Typical response of HEK 293 T cells exogenously expressing hTRPV3 to different concentrations of citronellal as indicated. Holding potential was −60 mV. Concentration–response curves of citronellal for activation of hTRPV3 after sensitization (WT: $EC_{50} = 5.78 \pm 0.72$ mM, $n_H = 3.76 \pm 1.39$, $n = 7$ cells). **d** Whole-cell hTRPV3 currents evoked by variable citronellal concentrations at 23 °C and 37 °C. Heat-evoked current traces were recorded in whole-cell configuration from hTRPV3-expressing HEK 293 T cells held at −60 mV. The temperature pulse (37 °C) is shown in red. Normalized concentration–response curves for hTRPV3 activation by citronellal at the indicated temperatures (at 23 °C: $EC_{50} = 5.77 \pm 0.51$ mM, $n_H = 3.84 \pm 1.03$, $n = 6$ cells; at 37 °C: $EC_{50} = 1.31 \pm 0.04$ mM, $n_H = 3.00 \pm 0.25$, $n = 6$ cells). **e** Statistical analysis of HaCaT cells viability under different concentrations of citronellal treatment. $n = 6$ replicates. **f** Representative images of HaCaT cells stained with Edu (green) and DAPI (blue) after vehicle or 0.5 mM citronellal incubation for 24 h. Scale bar is 55 μm. **g** Statistical analysis of HaCaT cell proliferation under different concentrations of citronellal treatment. $n = 6$ replicates. **h** Statistical analysis of HaCaT cells proliferation under each indicated treatment. $n = 6$ replicates. One-way ANOVA with LSD multiple comparisons test for statistical analysis in (**e**) and (**g**). Two-tailed unpaired t-tests were used for statistical analysis in (**h**). All the data are expressed as mean ± SEM; $^*P < 0.05$, $^{**}P < 0.01$, n.s stands for not significant.

Ca^{2+} that occurs upon TRPV3 channel activation, we postulated that calcium ions may act as downstream signals mediating the effects of citronellal. As expected, the promotion of keratinocyte proliferation by citronellal was not observed in the absence of calcium (Fig. 3h). Additionally, activation of TRPV3 was found to result in the release of TGF-α and subsequent activation of the EGFR[12]. As shown in Fig. 3h, the proliferation-promoting effect of 0.5 mM citronellal to HaCaT cells was abrogated upon the co-treatment of EGFR inhibitor, erlotinib (100 nM). These results suggest that Ca^{2+} influx and EGFR activation, which are mediated by TRPV3 activation, are responsible for citronellal-induced proliferation of the human keratinocyte line.

Citronellal activates TRPV3 by binding to the vanilloid site

To unmask the molecular mechanism of TRPV3 activation by citronellal, we employed cryogenic electron microscopy (cryo-EM) to determine the structure of the TRPV3-citronellal complex. Full-length wild-type hTRPV3 protein was exogenously expressed in the yeast *Pichia pastoris* and purified in detergent micelles. The protein was then successfully reconstituted into lipid nanodiscs composed of soybean polar lipids and membrane scaffold protein 2N2 (MSP2N2) circularized lipid nanodiscs (Supplementary Fig. 3a, b), and subjected to cryo-EM in the absence and presence of 10 mM citronellal. The application of cryo-EM single particle analysis yielded a 3.13 Å resolution map for the apo state TRPV3 ($hTRPV3_{Apo}$) and a 3.53 Å resolution map for citronellal-bound TRPV3 ($hTRPV3_{Citronellal}$) (Supplementary Fig. 3c, d, Supplementary Fig. 6). The $TRPV3_{Apo}$ map shows densities at the vanilloid site that resemble a one- head and two-tails structure, indicative of the presence of an annular lipid (Fig. 4a), which is modeled as a palmitoyloleoylphosphatidylcholine (POPC) according to the head group size (Fig. 4b). This site is formed by the S3, S4, and S4-5 linker from one subunit and the S5, S6 from another subunit (Fig. 4a). The $TRPV3_{Citronellal}$ structure has an overall architecture similar to the apo state, while displaying distinct non-protein densities located within the vanilloid site (Fig. 4c). The citronellal molecule is observed to fit precisely within this density, thereby revealing a ligand binding site (Fig. 4d).

The binding of citronellal in the cleft is maintained through a combination of van der Waals interactions and hydrophobic interactions as illustrated in our refined atomic model. The short side chain of A560 and the specific orientation of the side chain of L563 facilitate the accommodation of citronellal within the spatial constraints of the binding pocket. The hydrophobic side chains of V525 and L664 contribute to the stabilization of the aliphatic chain of citronellal, with the citronellal molecules situated between transmembrane helices at the subunit interfaces. Residue S576, located on the S4-5 linker, forms the lower part of the citronellal binding pocket (Fig. 4e, f). To validate the

https://doi.org/10.1038/s41467-025-58033-9

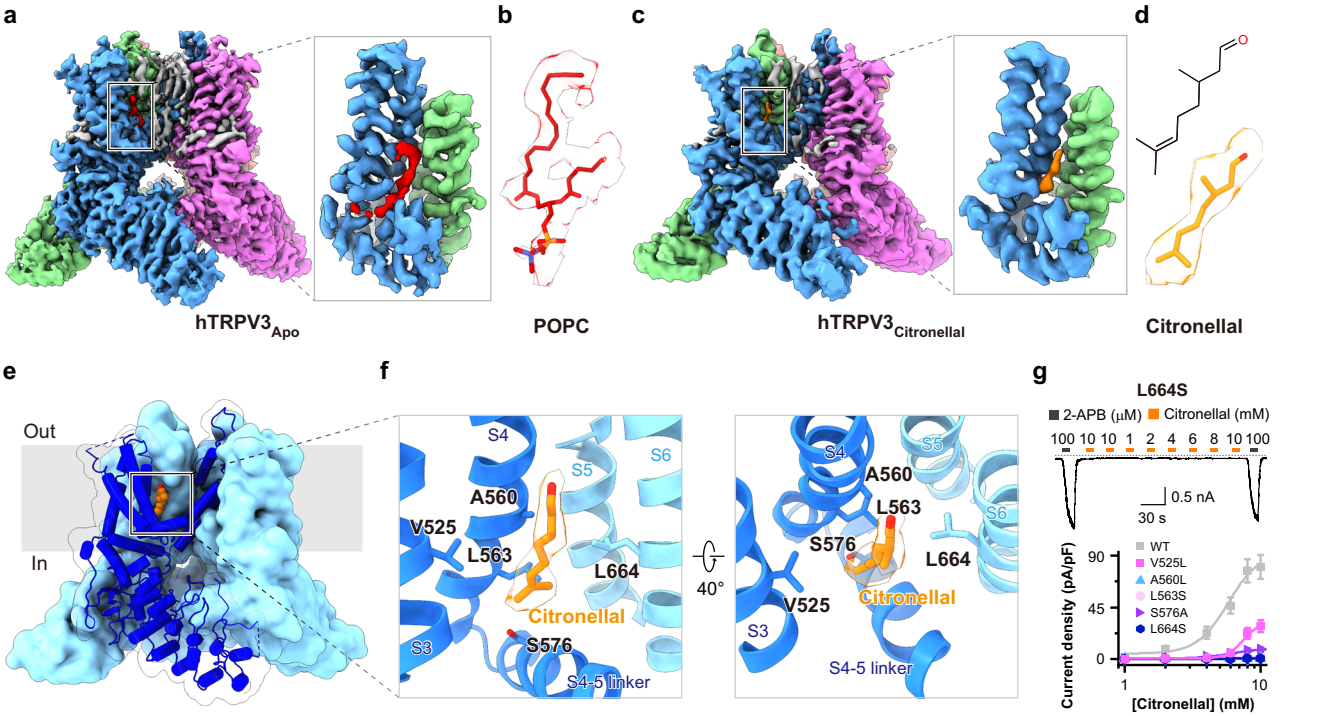

Fig. 4 | Citronellal activates TRPV3 by binding to the vanilloid site. a Cryo-EM reconstruction of the full-length wild-type human TRPV3 in ligand-free ($TRPV3_{Apo}$). The four subunits of a tetrameric channel protein are colored in four colors (blue, purple, salmon, green) with lipids densities (gray) shown. Close-up views of the vanilloid site in cryo-EM density map is shown in the box. In the $TRPV3_{Apo}$ map (**a**), a phosphatidylcholine (PC) lipid (red) occupies the vanilloid site of TRPV3. **b** Cryo-EM density of POPC (red surface). **c** Cryo-EM reconstruction of hTRPV3 bound to citronellal ($TRPV3_{Citronellal}$). In the $TRPV3_{Citronellal}$ map (**c**), citronellal (orange) is nested in the same pocket. **d** Chemical structure and cryo-EM density of citronellal (orange surface). **e** The overall structure of a $TRPV3_{Citronellal}$ tetramer. One chain is shown in blue cartoon and transparent surface, while the remaining three chains are shown as surface representations. **f** Expanded views of the citronellal binding pocket. The two adjacent chains are shown in dark blue and blue, respectively. The EM density of citronellal is represented by an orange transparent area. **g** A whole-cell recording of the hTRPV3-L664S mutant. The cell was exposed to different concentrations of citronellal, as indicated. Holding potential was −60 mV. Concentration–response curves of citronellal for activation of hTRPV3 mutants following full sensitization. Solid line indicates fits to the Hill equation with $EC_{50} = 5.78 \pm 0.72$ mM, $n_H = 3.76 \pm 1.39$ for WT ($n = 7$ cells); $EC_{50} = 6.25 \pm 0.57$ mM, $n_H = 3.61 \pm 0.84$ for S576A ($n = 7$ cells); and $EC_{50} = 5.08 \pm 0.36$ mM, $n_H = 3.81 \pm 0.95$ for L563S ($n = 6$ cells). Error bars represent SEM.

crucial interactions between TRPV3 and citronellal at the functional level, we performed systematic mutations of the residues in the citronellal-binding pocket of the hTRPV3 channel, as revealed by the structure, and performed whole-cell patch-clamp recordings to compare citronellal-evoked activation between WT and mutant TRPV3 channels. As shown in Fig. 4g, the A560L, L563S, and L664S mutations effectively abrogated the TRPV3 response to citronellal. 2-APB, which has been demonstrated to bind to distinct pockets of TRPV3 (Supplementary Fig. 7a), was used as a positive control to validate the functionality of the mutant channels. Furthermore, the activating potency of citronellal was significantly reduced for the V525L mutant and S576A mutant (max current density, WT: 80.18 ± 10.34 pA/pF; V525L: 28.72 ± 5.07 pA/pF; S576A: 8.35 ± 1.87 pA/pF).

Acyclic monoterpenes promote skin renewal by activating TRPV3 through binding to the vanilloid site

The above results unmask the structural mechanism by which citronellal activates TRPV3. Acyclic monoterpenes with a similar molecular structure to citronellal may also exert beneficial effects on the skin through comparable mechanisms. To test this hypothesis, we selected citral, linalool and isodihydrolavandulal (iso) derived from *Cymbopogon citratus*, *Cinnamomum camphora* and *Theobroma cacao* respectively for further investigation because these compounds possess a similar backbone and are used in daily care products[19] (Fig. 5a). The three compounds were indeed observed to activate hTRPV3 channels in a dose-dependent manner (Fig. 5b and Supplementary Fig. 4a). Fitting the dose-response curves with the Hill equation yielded an $EC_{50} = 6.61 \pm 0.93$ mM and $n_H = 3.08 \pm 1.06$ ($n = 8$) for citral, an $EC_{50} = 6.19 \pm 0.60$ mM and $n_H = 3.99 \pm 1.16$ ($n = 6$) for linalool, and an $EC_{50} = 6.54 \pm 0.5$ mM and $n_H = 3.78 \pm 0.83$ ($n = 7$) for iso (Fig. 5b).

Given the efficacy of citral, linalool, and iso in activating TRPV3, the subsequent objective was to ascertain whether all three compounds, akin to citronellal, facilitated skin renewal in mice. Similarly, as in the preceding experiments (Fig. 1a-h), 1% citral, 1% linalool and 1% iso were separately topically applied to the dorsal skin of WT and *Trpv3*$^{-/-}$ mice for a period of 3 weeks. As expected, the data illustrated that these treatments augmented epidermal thickness and keratin14 stratum thickness in WT mice but not in the *Trpv3*$^{-/-}$ group (Fig. 5c). Moreover, no discernible alteration was observed in skin dermal thickness and keratin10 stratum upon treatment among the different groups (Supplementary Fig. 4b, c).

We next sought to define the molecular determinant(s) of TRPV3 activation by these compounds. Similarly, we separately co-incubated hTRPV3 reconstituted into lipid nanodiscs with 8 mM citral, 10 mM linalool or 10 mM iso prior to sample preparation and subjected them to single-particle cryo-EM. After comprehensive classification and refinement, we were able to generate a high-resolution map for each of the complexes, with resolutions of 3.51 Å, 3.62 Å, and 3.39 Å, respectively (Supplementary Fig. 5a–c, Supplementary Fig. 6). The analysis demonstrated that the density maps for $TRPV3_{Citral}$, $TRPV3_{Linalool}$, and $TRPV3_{Iso}$ exhibited distinct non-protein densities within the vanilloid site, differing from those observed in the $TRPV3_{Apo}$ map. Importantly, these non-protein densities correspond to the ligands present in each

https://doi.org/10.1038/s41467-025-58033-9

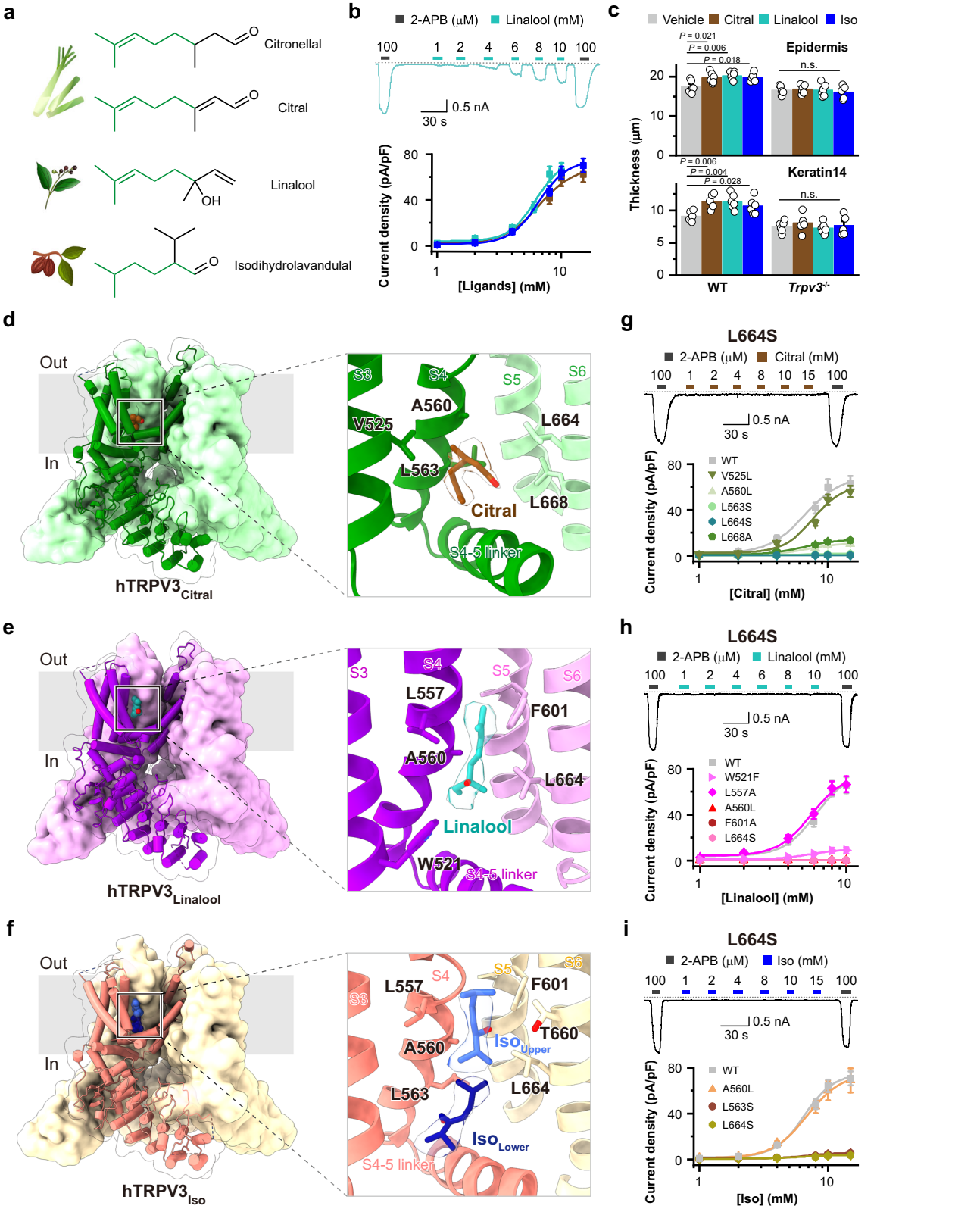

data set (Fig. 5d–f and Supplementary Fig. 5a–c). These findings indicate that these compounds interact directly with the vanilloid site of TRPV3.

The well-defined $TRPV3_{Citral}$ and $TRPV3_{Linalool}$ structures indicate that a single ligand occupies the vanilloid site, with a binding posture that is similar to that observed in the resolved $TRPV3_{Citronellal}$ structure. The binding of citral and linalool to the vanilloid site is facilitated by van der Waals interactions and hydrophobic interactions between the aliphatic chains of the ligands and the hydrophobic side chains of the channel protein, including L563, L664, and L668 for $TRPV3_{Citral}$ and L557, F601, and L664 for $TRPV3_{Linalool}$ (Fig. 5d, e). The introduction of mutations that reverse residue hydrophobicity or affect the hydrophobic surface of the binding pocket resulted in a significant reduction, and in some cases complete abolition, of ligand-evoked TRPV3

Fig. 5 | Citronellal-like acyclic monoterpenes activate TRPV3 by binding to the vanilloid site and promote skin renewal. a Chemical structures of citronellal, citral, linalool, and isodihydrolavandulal (iso) extracted from *Cymbopogon citratus*, *Cinnamomum camphora* and *Theobroma cacao*, respectively. **b** hTRPV3 activation evoked by linalool and concentration–response curves of whole-cell hTRPV3 currents evoked by acyclic monoterpenes at −60 mV. EC_{50} = 6.61 ± 0.93 mM, n_H = 3.08 ± 1.06 for citral (n = 8 cells); EC_{50} = 6.19 ± 0.6 mM, n_H = 3.99 ± 1.16 for linalool (n = 6 cells); and EC_{50} = 6.54 ± 0.5 mM, n_H = 3.78 ± 0.83 for iso (n = 7 cells). **c** Statistical analysis of epidermal and keratin14 stratum thickness of skin from WT and *Trpv3*$^{-/-}$ mice treated with vehicle, 1% citral, 1% linalool, and 1% iso for 3 weeks. n = 5 or 6 mice/group. Structure of $TRPV3_{Citral}$ (**d**), $TRPV3_{Linalool}$ (**e**), and $TRPV3_{Iso}$ (**f**) tetramers with ligands stained in brown for citral, teal for linalool, and royal blue and dark blue for iso. Expanded views showing citral (**d**), linalool (**e**), and iso (**f**) located in the binding pockets. Representative whole-cell recordings in TRPV3-L664S-expressing HEK 293T cells showing responses to different concentrations of citral (**g**), linalool (**h**), and iso (**i**), as indicated. Holding potential was −60 mV. Concentration-response curves of citral (**g**), linalool (**h**), and iso (**i**) for activation of hTRPV3 mutants. Citral: EC_{50} = 7.69 ± 0.97 mM, n_H = 3.76 ± 1.94 for V525L (n = 7 cells); EC_{50} = 7.06 ± 0.45 mM, n_H = 3.07 ± 0.51 for A560L (n = 7 cells); and EC_{50} = 6.52 ± 0.73 mM, n_H = 3.2 ± 0.89 for L668A (n = 6 cells); Linalool: EC_{50} = 5.92 ± 0.4 mM, n_H = 3.4 ± 0.58 for L557A (n = 7 cells); iso: EC_{50} = 6.88 ± 0.45 mM, n_H = 3.19 ± 0.55 for A560L (n = 7 cells); EC_{50} = 7.13 ± 0.41 mM, n_H = 3.61 ± 0.68 for L563S (n = 6 cells). Two-tailed unpaired t-tests were used for statistical analysis in (**c**). Data are presented as mean ± SEM; $^*P < 0.05$, $^{**}P < 0.01$, n.s stands for not significant.

currents (Fig. 5g, h). Notably, the W521F mutation affects linalool-induced TRPV3 activation but not that induced by citronellal or citral. This may be due to the van der Waals interactions brought by the bulky side chain of tryptophan and the formation of a putative hydrogen bond between the hydroxyl group of linalool and the indole ring nitrogen of W521 (Fig. 5e).

In contrast to the above three TRPV3-ligand complexes, each of which contains a single molecule occupying a single vanilloid site, the $TRPV3_{Iso}$ map revealed the presence of two molecules of iso in the vanilloid site. In accordance with their respective positions (Fig. 5f), the two molecules were designated "Iso_{Upper}" and "Iso_{Lower}". To elucidate the mechanism by which these two iso molecules activate TRPV3, residues in close proximity to both ligands were subjected to site-directed mutagenesis and subsequently evaluated for their functional impact. Electrophysiological data indicated that the mutants related to iso_{Upper}, including L557S, F601A, and T660A, had a limited effect on iso-evoked TRPV3 activation (Supplementary Fig. 8). With respect to iso_{Lower}, it was observed that the L563S and L664S mutants exhibited a significant reduction in the responses to iso (Fig. 5i). Specifically, the maximum current density for the WT was 70.75 ± 5.93 pA/pF (n = 7), whereas the L563S and L664S mutants exhibited a reduction to 5.71 ± 0.99 pA/pF (n = 6) and 3.65 ± 0.72 pA/pF (n = 8), respectively. These results suggest that binding of iso to the lower position of the vanilloid site is responsible for TRPV3 activation.

Acyclic monoterpenes competitively displace endogenous lipids from the vanilloid site, thereby inducing conformational rearrangements

The gating mechanism of ligand-gated channels is distinguished by its capacity for precise ligand recognition, regulatory alterations in the interactions between the channel protein and the native lipid environment, and sophisticated conformational changes of the channel protein[26–29]. Using a nanodisc reconstitution strategy that mimics the cellular membrane environment, EM densities of POPC were better observed in the transmembrane domain of TRPV3. In the $TRPV3_{Apo}$ structure, it was observed that Q695, which has a polar side chain on the TRP helix, formed a hydrogen bond with the vanilloid site-POPC (Fig. 6a, b). In contrast, the liganded TRPV3 structures demonstrated the absence of the endogenous lipid POPC (Supplementary Fig. 9a, b), indicating that essential oil displacement of the endogenous lipids is a requisite phenomenon. To substantiate this assertion, we proceeded to construct Q695L and Q695R mutants for a comprehensive analysis. As illustrated in Fig. 6b, c, the substitution of glutamine (Q) by leucine (L) to disrupt the hydrogen bond formed between the TRPV3 channel protein and POPC resulted in a significant increase in the potency of acyclic monoterpenes activation. In response to citronellal, iso, linalool, and citral, respectively, the EC_{50} value decreased from 5.78 ± 0.72 mM, 6.54 ± 0.5 mM, 6.19 ± 0.60, 6.61 ± 0.93 mM for WT to 0.45 ± 0.06 mM, 0.78 ± 0.01 mM 0.42 ± 0.02 mM, 0.44 ± 0.01 mM for Q695L (Fig. 6d, Supplementary Fig. 9c, d). Conversely, the mutation of Q659 to R may facilitate the formation of a hypothetical hydrogen bond with POPC, thereby enhancing the interaction between the channel protein and POPC and rendering it insensitive to essential oil ligands (Fig. 6c, d and Supplementary Fig. 9c, e).

To further investigate the relationship between POPC and essential oil ligands within the same vanilloid binding pocket, we performed patch-clamp recordings and found that POPC inhibited citronellal-evoked currents in a dose-dependent manner (Supplementary Fig. 9f). However, due to its limited solubility, the highest of POPC concentration was 100 μM in our electrophysiological recordings. Intriguingly, the inhibitory efficacy of POPC was more effective with decreasing citronellal concentration, e.g., the presence of 100 μM POPC inhibited TRPV3 currents elicited by 4 mM or 10 mM citronellal to 41.9 ± 8.6% and 14.6 ± 1.7% of control levels, respectively (Supplementary Fig. 9f, g). In contrast, no inhibition was observed in Q695L mutant, due to the disruption of the lipid-channel protein interaction (Supplementary Fig. 9f, g). Consistently, the inhibition ratio of 100 μM POPC progressively decreased with increasing citronellal concentration, which differed from the relatively consistent inhibition ratio of dyclonine upon citronellal activation, a selective inhibitor of TRPV3[23] (Supplementary Fig. 9h, i). These results thus support the competitive binding relationship between essential oil ligands and POPC.

The opening of gated ion channels from a closed state to an open state is contingent upon a conformational change in the pore region, which enables the passage of ions in or out. The MOLE program was employed to calculate the pore profiles for all five protein structures, with an extensive comparison subsequently conducted. As depicted in Fig. 6e, the pore profiles of $TRPV3_{Citronellal}$, $TRPV3_{Iso}$, and $TRPV3_{Linalool}$ exhibit remarkable similarities. The upper selectivity filter (SF) restriction is defined by the main-chain carbonyl oxygens of G638, while the lower gate restriction is formed by the side chains of I674 on the π-helix containing S6. In the three structures with bound ligands, the lower gate shows an expansion from 5.4 Å in the apo form to 5.8 Å, 5.5 Å, and 6.9 Å, respectively. In contrast to $TRPV3_{Citronellal}$, the S6 of $TRPV3_{Citral}$ is completely α-helical, with the lower gate restriction derived from M677 rather than I674. The diagonal distance and pore profile of $TRPV3_{Citral}$ are distinct from those of $TRPV3_{Apo}$. In addition to the pore regions, four liganded structures represent different states of the TRPV3 channel protein that are distinct from the apo state within its gating cycle. $TRPV3_{Citronellal}$, $TRPV3_{Iso}$ and $TRPV3_{Linalool}$ structures are characterized by an upward shift of approximately 5 Å and a clockwise rotation of 8° (viewed from the intracellular side) of the ARDs, a transition of the C-terminal coil to a helix, and the observation of an N-terminal coil, all of which are similar to other sensitized and open TRPV3 structures[28,30–32] (Supplementary Fig. 10a–c). Cytoplasmic domain of $TRPV3_{Citral}$ exhibits a C-terminal coil and unshifted and unrotated ARDs, similar to the apo conformation, resembling inactivated TRPV3 structures[30] (Supplementary Fig. 10a–c). Following ligand binding and lipid displacement, the vanilloid site function as the primary initiator of conformational changes. The S2-3 linker undergoes a significant degree of movement, which is caused by the formation of

https://doi.org/10.1038/s41467-025-58033-9

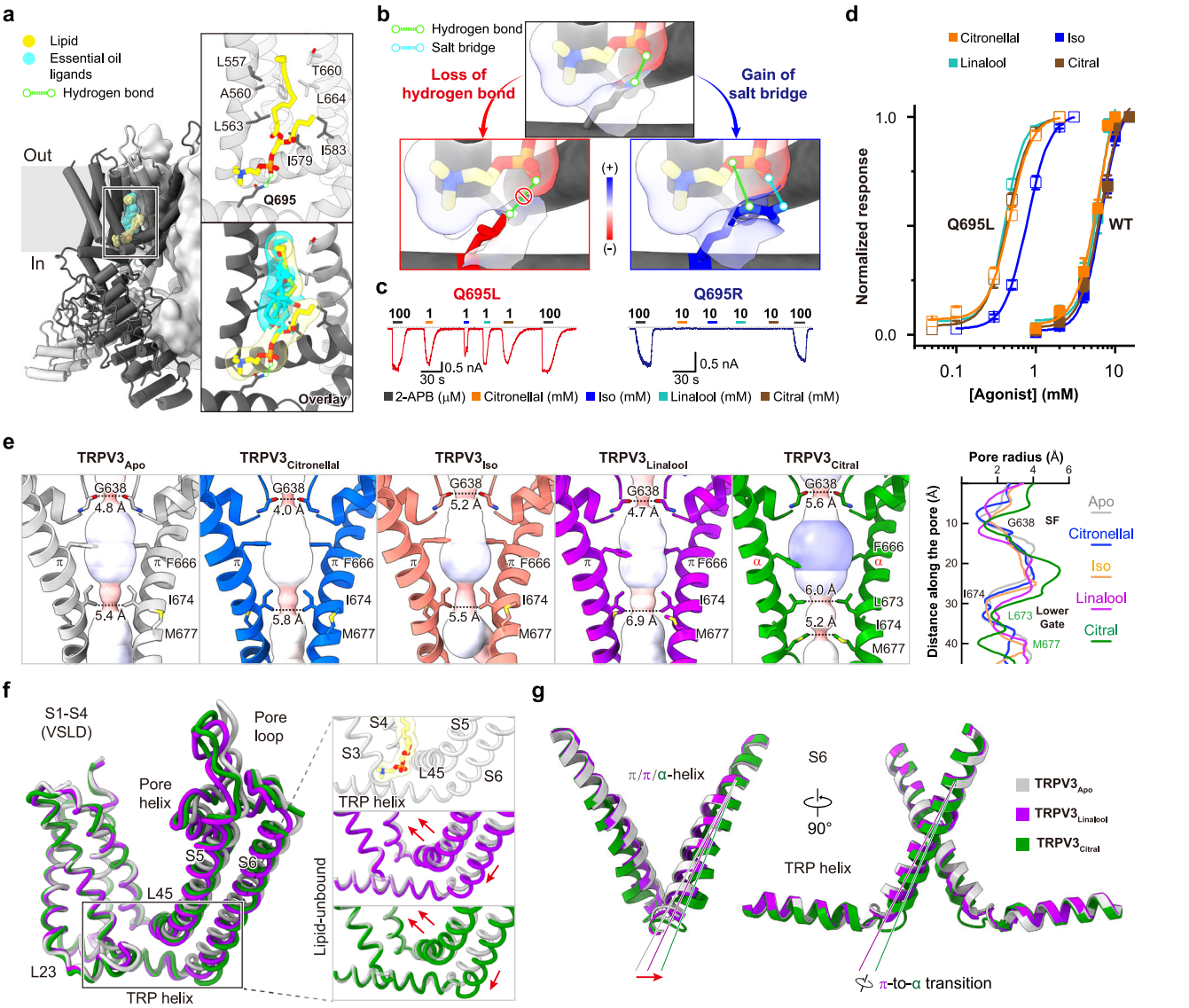

Fig. 6 | Natural acyclic monoterpenes activate TRPV3 by competitive displacement of endogenous lipids from the vanilloid site. a The apo or ligand-bound TRPV3 structures were overlaid with endogenous lipid or acyclic monoterpene molecules bound in the vanilloid site. In the overlay view, lipids and ligands are shown as sticks with transparent surfaces, indicating the overlapping binding position. In the $TRPV3_{Apo}$ structure, the putative hydrogen bond between Q695 and POPC is indicated as a dashed line. **b** The electrostatic surfaces of the lipid and residues Q695, L695, and R695 are shown. Hydrogen bond and salt bridge interactions are indicated by black and green dashed lines, respectively. **c** hTRPV3 Q695L and Q695R mutants' responses to acyclic monoterpenes. Holding potential was −60 mV. **d** Normalized concentration-response curves for hTRPV3 activation by essential oil ligands. Citronellal: EC_{50} = 5.78 ± 0.72 mM, n_H = 3.76 ± 1.39 for WT (n = 7 cells); EC_{50} = 0.45 ± 0.06 mM, n_H = 3.18 ± 1.31 for Q695L (n = 7 cells); iso-dihydrolavandulal (iso): EC_{50} = 6.54 ± 0.5 mM, n_H = 3.78 ± 0.83 for WT (n = 7 cells); EC_{50} = 0.78 ± 0.01 mM, n_H = 3.01 ± 0.06 for Q695L (n = 6 cells); linalool: EC_{50} = 6.19 ± 0.6 mM, n_H = 3.99 ± 1.16 for WT (n = 6 cells); EC_{50} = 0.42 ± 0.02 mM, n_H = 3.82 ± 0.72 for Q695L (n = 7 cells); citral: EC50 = 6.61 ± 0.93 mM, nH = 3.08 ± 1.06 for WT (n = 8 cells); EC_{50} = 0.44 ± 0.01 mM, nH = 3.13 ± 0.33 for Q695L (n = 6 cells). **e** The ion-conducting pores of TRPV3 structures are depicted as gray spheres, calculated with MOLE. For clarity, only two opposing subunits of pore domains are shown. Diagonal distances are shown as dashed lines, and gating residues at selectivity filters and lower gates are labeled. Superimposed structures of $TRPV3_{Apo}$, $TRPV3_{Linalool}$ and $TRPV3_{Citral}$, showing only the transmembrane domains (**f**). Domains and transmembrane helices are labeled, and red arrows in the expanded views indicate conformational changes due to acyclic monoterpenes expelling endogenous lipids. Movements of S6-TRP helices (**g**) are indicated by red arrows.

hydrogen bonds between S518 and main-chain atoms (Supplementary Fig. 10d). The introduction of mutations, including S518A, S518F and L517F, which disrupt the interactions or the linker conformation, resulted in the impairment of channel coupling. This, in turn, led to the failure of acyclic monoterpene-evoked TRPV3 activation (Supplementary Fig. 10e, f).

In $TRPV3_{Apo}$, the presence of two acyl chains of the annular lipid wedged in the gap formed by the S2-3 linker, S3, and the S4-5 linker, maintained the spacing and conformation of the S2-3 linker. Removal of endogenous inhibitory lipids created space for the S4-5 linker to move away from the central axis of the channel pore, resulting in increased mobility in the pore region (Fig. 6f). The S6-containing π-helix dilates, thereby facilitating the permeation of cations. The π-to-α transition results in both twisting and dilation of S6, which may contribute to the inactivation of the TRPV3 channel protein (Fig. 6g).

Collectively, our results demonstrate that the lipophilic acyclic monoterpenes access TRPV3 vanilloid sites within the lipid bilayer by competitively displacing the endogenous lipids, thereby triggering the stepwise conformational changes of the TRPV3 channel protein leading to activation.

Discussion

Acyclic monoterpenes, renowned for their aromatic essence, are widely used for skin healthcare. This study elucidates the beneficial effects of essential oils on skin health and delineates their molecular mechanisms. Topical application of essential oils in vivo was observed to enhance skin regeneration by promoting keratinocyte proliferation (Supplementary Fig. 11). Our results identify TRPV3 as the molecular target of citronellal, linalool, citral and isodihydrolavandulal. Furthermore, we have unveiled the structural basis underlying the activation of TRPV3 by essential oil agonists. The results indicate that essential oil agonists interact with several key residues (L664, L563, A560) in the vanilloid binding pocket by displacing the lipid molecule, inducing changes in the channel protein conformation, and ultimately leading to TRPV3 channel activation (Supplementary Fig. 11 and Supplementary Movie 1).

Although plant-derived essential oils have been shown to have skin repair and anti-aging properties[33,34], the precise mechanism of action remains largely unknown. In this study, we reveal a class of acyclic monoterpenes, including citronellal, that promote skin regeneration by targeting the TRPV3 channel, which is highly expressed in keratinocytes. Previous research has demonstrated that several monoterpenes activate the TRPV3 channel[35], with carvacrol being a commonly used agonist for TRPV3, but its non-specificity is a drawback as it has effects on other TRP channels[36,37]. Furthermore, in vivo studies have shown that carvacrol causes itching[38] and induces skin irritation[15], which may restrict its potential applications in skin care products. Maintaining optimal levels of TRPV3 activity is necessary for skin health. Deficiency or excessive activation of TRPV3 has been linked to pathological degeneration[13,18]. It is imperative to recognize that varying concentrations of citronellal can produce different and occasionally contradictory effects on the skin. Our in vivo results indicate that a concentration of 1% citronellal is conducive to skin renewal. Conversely, 10% citronella oil has been demonstrated to potentially induce sensitization and irritation[5]. In vitro studies have demonstrated that citronellal, when tested at a concentration range of 0.2–0.5 mM, has the potential to effectively promote HaCaT proliferation at 37°C. However, when citronellal concentrations exceeded 1 mM at 37 °C, the results indicated an inhibitory effect on HaCaT proliferation.

In order to elucidate the mechanism by which citronellal promotes skin renewal, we examined the expression of growth factors in keratinocytes. Activation of TRPV3 may facilitate the release of TGF-α from keratinocytes, which in turn increases the phosphorylation of EGFR. In physiological processes, TRPV3, in conjunction with the TGF-α/EGFR complex, plays a crucial role in regulating hair morphogenesis, maintaining skin barrier integrity, and controlling keratinocyte proliferation[10,12]. Given the marked elevation of TGF-α in the citronellal-treated groups, it can be postulated that TGF-α plays a pivotal role in citronellal-induced skin regeneration. Since TRPV3 has been demonstrated to regulate Smad2/3 pathways known to mediate TGF-β action[39,40], it is plausible that a TRPV3-Smad-TGF-β axis may exist. The data demonstrate that citronellal increases TGF-β expression in wild-type mice but not in *Trpv3*$^{-/-}$ mice, indicating that TRPV3 activation in keratinocytes may facilitate TGF-β release and thereby promote skin renewal. Furthermore, the results illustrate that citronellal, through TRPV3 activation, enhances VEGF expression and contributes to skin rejuvenation. While there is currently no direct evidence linking TIMP1 as a downstream signaling molecule of TRPV3, our findings suggest a potential link between the two that merits further investigation.

To elucidate the molecular basis of TRPV3 gating, cryo-EM structures have been made available in elucidating the binding sites of TRPV3 modulators, including dyclonine[41], the plant-derived coumarin osthole[42], trpvicin[43], 2-APB[26–28] and tetrahydrocannabivarin (THCV)[44]. Nevertheless, the structural data of the activated TRPV3 channel are currently limited. In this study, we have uncovered the binding of four plant-derived acyclic monoterpenes to TRPV3 vanilloid site, and illustrated the structural basis of the ligand-protein interactions. The backbone of acyclic monoterpenes is a chain-like structure formed by the polymerization of dimolecular isoprene, which confers hydrophobic and lipophilic properties to these compounds. Consistent with this, a general hydrophobic environment within the TRPV3 vanilloid site mediates the binding of acyclic monoterpenes ligands, rather than a strong coordination of the common structural backbone of these ligands (Supplementary Fig. 7b, c). The key determinants, including A560, L563, and L664, constitute an extensive hydrophobic surface within the binding pocket, while other polar interactions facilitate precise ligand recognition. As a result, a variety of binding modes have been observed for structurally analogous ligands. Notably, the $TRPV3_{Iso}$ structure exhibited two molecules within a single vanilloid site, which can be attributed to the shorter and globular posture of the iso molecules, differing from those of citronellal, citral, and linalool. In conjunction with the functional study, it was determined that iso activates the TRPV3 channel by occupying the lower portion of the pocket.

The transmembrane domains of the tetrameric TRP channels share a similar architectural configuration, resulting in the presence of an orthosteric vanilloid binding pocket (VBP) composed of the S3, S4, S4-5 linker, and TRP helix of one subunit and the S5 and S6 of an adjacent subunit. The presence of annular lipids and cholesterol within the vanilloid binding pocket of TRPV1 and TRPV2 has been shown to exert a negative regulatory effect on channel function[45–47]. Similar to our structural findings on TRPV3 channel protein using lipid nanodisc strategy, it has also been reported that the TRPV3 vanilloid site harbors annular lipids in structures determined in detergents, strongly suggesting that the channel protein intricately interplays with endogenous lipids within the native cytoplasmic membrane[30,31,48]. Our structure-based functional analysis further revealed the effects of lipids and ligands within the TRPV3 vanilloid site, indicating that lipid expulsion is an essential step in channel opening. Interestingly, among these acyclic monoterpenes, isodihydrolavandulal shows a relatively weaker ability to activate TRPV3, as indicated by a higher EC_{50}. This may correspond to the weaker pore dilatation of the $TRPV3_{Iso}$ structure and imply that stronger activation induces a larger pore opening of the TRPV3 channel. As both endogenous lipids and exogenous modulators regulate TRP channel function via the orthogonal vanilloid site, the pocket represents a key area of interest for functional studies and drug design. Our analysis of the TRPV3 vanilloid site therefore provides a general framework for understanding the interactions between lipids, ligands, and channels during the gating process, as well as valuable structural information that can inform further rational drug design.

Upon the expulsion of lipids from the vanilloid site by acyclic monoterpenes, a series of conformational rearrangements were observed, including those of the S2-3 linker, NC termini, and ARDs. Four liganded structures exhibit analogous properties in these regions and diverge from $TRPV3_{Apo}$. Our functional analysis of specific interactions at the S2-3 linker has revealed its importance in channel coupling. In the direction away from the pore, this region may exert its coupling function by transmitting a conformational wave to the cytoplasmic domain, thereby facilitating channel gating from a distal region. The relatively lower local resolution of the S2-3 linker region suggests that it exhibits high dynamics during channel gating, which aligns with our hypothesis (Supplementary Fig. 6a). A similar phenomenon was also observed in heat-treated TRPV3 structures, suggesting that the conformational change is critical for channel gating in response to different types of stimuli.

TRPV3 activation by essential oil ligands is analogous in conformational rearrangements to the effects of classical agonists within the TRPV1 VBP, namely capsaicin and resiniferatoxin (RTX).

The binding of low-molecular-weight acyclic monoterpenes exhibits a major dependence on van der Waals interactions and hydrophobic interactions, resulting in a relatively low affinity for the channel, which differs from the high affinity of TRPV1 VBP agonists due to extensive polar and hydrophobic interactions[45,49–52]. In addition, the space vacated by the displacement of endogenous lipids, was re-occupied by R567 and uncharged Q580 (in TRPV3) rather than R557 and charged E570 (in TRPV1)[45,46,53]. This weaker interaction between two residues in TRPV3 suggests that the binding of essential oils exerts a weaker coupling to the pore domain. Absent and overactive TRPV3 channel function both result in skin defects, however, the mild activation of TRPV3 induced by essential oil ligands, leads to beneficial effects on skin physiology.

$TRPV3_{Citronellal}$, $TRPV3_{Iso}$, and $TRPV3_{Linalool}$ are characterized by expanded ion permeation pathway, π-bulge-containing S6 helices, shifted and rotated ARDs and α-helical C-terminus. These structures resemble a sensitized state proposed by Nadezhdin et, al. and determined in MSP2N2 nanodiscs under temperature stimulus[31]. Whereas in $TRPV3_{Citral}$, an entirely α-helical S6 with M677 forming the lower restriction was observed, confirming previously determined inactivated structures[28,32]. The extent of dilation and the conformation of the S6 could be influenced by several factors, including different properties of the ligands, the in vitro conditions used during structure determination, and the dynamic behavior of the ion channel itself. Therefore, structures in different states were generated from the datasets, revealing the intricate and fine-tuned nature of channel gating. These newly determined structures further advance our understanding of TRPV3 channel gating.

In conclusion, our findings indicate that acyclic monoterpenes serve as important molecular instruments for the innovation of targeted TRPV3 modulators. This helps to advance our understanding of the TRPV3 channel gating mechanism, pharmacology, and physiological implications in healthcare contexts.

Methods

Ethics

All the experiments were conducted in accordance with protocols approved by the Institutional Animal Care and Use Committee of Wuhan University (Approval NO. WDSKY0201804) and adhered to the Chinese National Laboratory Animal-Guideline for Ethical Review of Animal Welfare.

Evaluation of dermatological effects of plant essential oils in mice

These experiments were performed on 5-week-old female wild-type and *Trpv3*$^{-/-}$ C57BL/6 mice. *Trpv3*$^{-/-}$ mice were kindly provided by Dr. Zhenyu Cao from China Pharmaceutical University[23]. Mouse genotypes were determined by nested PCR analysis of tail DNA, and the first-step primers are as follows, forward 5′- AGGGAGGGAGGTAGGGAGGT-3′, and reverse 5′- CAGGATGCACCGCAGCCCCACTGGT -3′. The products of the first step were then used as templates and reacted with the second-step primers: 5′-ACACGAGTTGTCTGGGTGGC-3′ and 5′-CGATGACGAGCTGAACAAAGTC-3′. Finally, the second-step products were identified by gene sequencing. To assess the dermatological effects of citronellal, the dorsal skin of mice was shaved with an electric clipper and hairs were depilated using a commercial depilatory cream (Veet, London, England). The solution, comprising essential oils (1%) or normal saline (0.9% NaCl), dissolved in a mixture of ethanol (10%) and Tween80 (1%), was topically applied to the dorsal skin of the mice twice daily for periods of one, two, or three weeks. At the end of the treatment period, the mice were euthanized and subjected to the following analyses. To ensure the highest standards of animal welfare and to reduce the number of animals used, the treated skin area was bisected. One half was used for cytokine detection, and the other half for histological examination.

All mice were housed in the special pathogen-free animal facility at Wuhan University with a 12 h dark/12 h light cycle and maintained on standard chow and water. Animals were euthanized with CO_2 and subjected to various studies.

cDNA constructs, cell culture and gene expression

The full-length cDNA of mTRPV1 (NM_001001445.2), mTRPV2 (NM_001382489.1), mTRPV3 (NM_145099.3), mTRPA1(NM_177781.5), rTRPV4 (NM_023970.1), and rTRPM8 (NM_134371.3) were gifts from Dr. Feng Qin (State University of New York at Buffalo, Buffalo). The plasmid encoding the full-length hTRPV3 (NM_001258205.2) was kindly provided by Dr. Zengqin Deng from the Wuhan Institute of Virology, Chinese Academy of Sciences. All mutations were generated by the overlap-extension polymerase chain reaction (PCR) method[54]. Primer sequences are listed in Supplementary Table 1. All primers were ordered from Sangon Biotech. The resulting mutations were then verified by DNA sequencing. HaCaT and HEK 293 T cells were grown in Dulbecco's modified Eagle's medium (DMEM, Thermo Fisher Scientific, MA, USA) containing 10% heat-inactivated fetal bovine serum (FBS), 50 units/mL penicillin, and 50 mg/mL streptomycin, and incubated at 37 °C in a humidified incubator (Thermo Fisher Scientific, MA, USA) gassed with 5% CO_2. HEK 293T cells, obtained from ATCC (Cat# CRL-3216), when grown to ~80% confluence were transiently transfected with the desired DNA constructs using polyethylenimine (PEI, Polysciences, Inc., Warrington, USA) or Lipofectamine 2000 (Invitrogen) according to the manufacturer's instructions. Transfected HEK 293 T cells were reseeded on 12 mm round glass coverslips coated with poly-L-lysine. Subsequent electrophysiological or Ca^{2+} imaging experiments were performed 24-48 h after transfection.

Mouse epidermal keratinocyte culture

Briefly, newborn wild-type C57B/6 mice (postnatal days 1–3) were deeply anaesthetized and decapitated, and immersed in 10% povidone-iodine, 70% ethanol, and phosphate-buffered saline for 5 min, respectively. The skin on the back was removed and rinsed with pre-cold sterile phosphate-buffered saline (PBS) in a 100-mm Petri dish and transferred to a 2-ml tube filled with pre-cold digestion buffer containing 4 mg/ml Dispase II and incubated overnight at 4 °C. After treatment with dispase II for 12–18 h, the epidermis was carefully separated from the dermis, mechanically disaggregated, and filtered through a 70-μm filter. Keratinocytes were dispersed by gentle scraping and rinsed with KC growth medium (Invitrogen, Carlsbad, CA). The resulting suspension of single cells was collected by centrifugation, and the cells were seeded onto poly-L-lysine-precoated coverslips, and maintained in the defined keratinocyte serum-free medium (K-SFM; Gibco, MA, USA) supplemented with 0.06 mM Ca^{2+}. Patch clamp and calcium imaging experiments were conducted 12 h after plating. Immunofluorescence experiments were typically performed 24–48 h after plating.

Ca^{2+} imaging

The Ca^{2+} imaging experiments were performed according to the protocol established by Mo et al.[55]. Briefly, cells on coverslips were loaded with 2 μM Fluo-4 AM (Beyotime Bio-Tech Co., Ltd.) for 30 min at 37 °C in the original culture room. The cells were then washed three times with an incubation buffer containing (in mM) 140 NaCl, 5 KCl, 2 $MgCl_2$, 10 HEPES, 10 glucose, and 2 $CaCl_2$ (pH 7.4). Cells were incubated in incubation buffer for 30 min at 37 °C to allow de-esterification of intracellular AM esters. Calcium imaging was performed on an inverted epifluorescence microscope (Olympus IX 73) equipped with a complete illumination system (Lambda XL, Sutter Instruments). Fluorescent images were acquired using a cool CCD camera (Cool SNAP ES2, Teledyne Photometrics) controlled by Micro-Manager 1.4 (Vale lab, UCSF) using a public 1394 digital camera driver (Carnegie Mellon University). Images were acquired at 448-492 nm excitation and 512-

630 nm emission in a continuous time-based mode. After taking baseline images, different treatments were applied. The bath solution containing 1 μM ionomycin (Med Chem Express, NJ, USA) was applied at the end of each experiment to ascertain cell viability. More than 90% of the cells were responsive to ionomycin stimulation and were included in the analysis. Analytical calculations of fluorescence intensity changes were designated as $\Delta F/F_0 = (F - F_0)/F_0$, where F represents the peak intensity elicited by the agonist within the region of interest, and F_0 represents the baseline intensity.

Cell viability analyzed by flow cytometry

HaCaT cells, gifted by Professor Liu Yu from Wuhan University, were cultured and propagated in 24-well plates and treated with the indicated compounds for 24 h. After the treatment, the cells were enzymatically dissociated with trypsin, resuspended in phosphate-buffered saline (PBS), and labeled with Calcein AM (Beyotime, China, catalog:2012) according to the manufacturer's instructions. Cell viability was then quantified using a Beckman flow cytometer (CytoFlex), operated with CytExpert software (Beckman Coulter Life Sciences, CA, USA).

Cell proliferation assay

The cell proliferation assay was conducted according to the protocol provided by Beyotime Biotechnology (Shanghai, China). HaCaT cells were cultured on 24-well coverslips until they reached 70–80% confluence. The cells were then exposed to essential oils alone or in combination with dyclonine for a period of 24 h. The cells were then incubated with Edu-488 buffer for 2 h, subjected to a reaction with an auxiliary solution, fixed with 4% paraformaldehyde, and stained with DAPI. Fluorescence images were captured using a Leica Microsystems Thunder Imaging DMI8 microscope (Wetzlar, Germany). Images were analyzed using ImageJ (1.43 m). Quantities of DAPI and Edu-positive cells were obtained within blue or green-specific channels, respectively. The number of DAPI/EdU double-positive cells was determined by analyzing overlay images generated from both channels. The cell proliferation rate was calculated as the ratio of DAPI/EdU double-positive cells to DAPI-positive cells. Each treatment group consisted of six replicates.

RT-PCR and qPCR

Total RNA was isolated from mouse skin samples using TRIzol reagent (Takara, Osaka, Japan), and its purity and concentration were determined spectrophotometrically (Eppendorf, Hamburg, Germany). The extracted RNA was then reverse transcribed using AMV reverse transcriptase (Monad, Suzhou, China). Gene expression was examined on a Bio-Rad CFX Connect system using a rapid two-step amplification program with 2x SYBR Green Master Mix (Bio-Rad Laboratories, CA, USA). The value obtained for each gene was normalized to that of the gene encoding GAPDH. Primer sequences are listed in Supplementary Table 2. All primers were ordered from Sangon Biotech.

Electrophysiological recording

Conventional whole-cell and excised patch-clamp recording methods were used. For the recombinant expression system, green fluorescent EGFP was used as a surface marker for gene expression. Patch-clamp recordings were voltage-clamped using an EPC10 amplifier with the Patchmaster software (HEKA, Lambrecht, Germany). For a subset of recordings, currents were amplified using an Axopatch 200B amplifier (Molecular Devices, Sunnyvale, CA) and recorded through a BNC-2090/MIO acquisition system (National Instruments, Austin, TX) with QStudio developed by Dr. Feng Qin at the State University of New York at Buffalo. Recording pipettes were pulled from borosilicate glass capillaries (World Precision Instruments), and fire-polished to a resistance between 2 and 4 MΩ when filled with an internal solution. Whole-cell recordings were typically sampled at 5 kHz and filtered at 1 kHz, and single-channel recordings were sampled at 25 kHz and filtered at 10 kHz. The compensation of pipette series resistance and capacitance were compensated using the built-in circuitry of the amplifier (>80%) to reduce voltage errors.

For recordings in keratinocytes, the bath solution consisted of (in mM) 140 NaCl, 5 KCl, 2 $MgCl_2$, 2 $CaCl_2$, 10 glucose, 10 HEPES, pH 7.4 adjusted with NaOH and the pipette solution contained (in mM): 140 CsCl, 5 KCl, 3 EGTA, and 10 HEPES, pH 7.3 adjusted with CsOH. For recordings of expressed TRP channels other than TRPV4, the bath solution consisted of (in mM): 140 NaCl, 5 KCl, 3 EGTA, and 10 HEPES, with pH adjusted to 7.4 with NaOH. The pipette solution in the experiment contains (in mM): 140 CsCl, 5 KCl, 3 EGTA, and 10 HEPES with pH 7.4 titrated with CsOH. For TRPV4 channel recording, the bath solution contained (in mM): 135 NaCl, 5 CsCl, 1 $MgCl_2$, 1 $CaCl_2$, 10 Glucose, 10 HEPES, pH 7.4 adjusted with NaOH and the electrodes were filled with (in mM): 130 CsCl, 5 EGTA, 5.5 $MgCl_2$, 5 Na_2ATP, and 5 HEPES titrated to pH 7.4 with CsOH. For excised patches, symmetric solutions consisted of (in mM) 140 NaCl, 5 KCl, 3 EGTA and 10 HEPES with pH 7.4 were used. The exchange of external solution was performed using a gravity-driven local perfusion system. As determined by the conductance tests, the solution around a patch under study was completely controlled by the application of a flow rate of 100 μl/min or greater.

Citronellal was purchased from Macklin (Shanghai, China), while melonal, isodihydrolavandulal, citral, and linalool were purchased from Aladdin (Shanghai, China). All other reagents, unless otherwise stated, were obtained from Sigma Aldrich (Merck, Darmstadt, Germany). Water-insoluble reagents were dissolved in pure ethanol or DMSO to make a stock solution and diluted to the desired final concentrations in the recording solution before the experiment. The final concentrations of ethanol or DMSO did not exceed 0.3%, which had no effect on currents.

Ultrafast temperature jump

Rapid temperature jumps were generated by laser irradiation from a single emitter infrared laser diode (1470 nm) as the heat source[23]. A multimode fiber with a core diameter of 100 μm was used to transmit the launched laser beam. The other end of the fiber exposed to the fiber core was placed close to cells as the perfusion pipette is typically positioned. The laser diode driven by a pulsed quasi-CW current powder supply (Stone Laser, Beijing, China). Pulsing of the controller was controlled from computer through the data acquisition card using QStudio software developed by Dr. Feng Qin at State University of New York at Buffalo. A blue laser line (460 nm) was coupled into the same fiber to aid alignment. The beam spot on the coverslip was identified by the illumination of GFP-expressing cells using the blue laser during the experiment. Constant temperature steps were generated by irradiating the tip of an open pipette filled with the bath solution and the currents through the electrode were used as a readout for feedback control. Temperature was calibrated offline from the electrode current based on the temperature dependence of electrolyte conductivity.

Immunofluorescence

Cells, designated as primary keratinocytes or HaCaT cells, were cultured on poly-L-lysine-coated coverslips. Following three consecutive washes with phosphate-buffered saline (PBS), the cells were fixed with 4% paraformaldehyde (PFA) for 20 minutes. After fixation, the sections or cells were blocked with 5% goat serum for 15 min at room temperature, followed by incubation with primary antibodies (detailed in Supplementary Table 3) overnight at 4 °C. Samples were then incubated with the corresponding secondary antibodies, and the nuclei were stained with DAPI. Imaging was performed using a fluorescence scanning microscope (Leica Microsystems, Thunder Imaging DMI8, Wetzlar, Germany) with LAS AF Lite sofeware (Leica Microsystems).

Histological analysis

Following transcardial perfusion with 4% paraformaldehyde (PFA), skin regions subjected to chemical treatment were harvested and fixed in

the same solution overnight. The tissues were then dehydrated in a graded ethanol series, embedded in paraffin, and sectioned at a thickness of 5 μm using a microtome. General morphological assessment was performed on the sections stained with hematoxylin and eosin (H&E) according to standard protocols. Immunohistochemical analysis was conducted to assess the expression of keratin14 and keratin10, using primary and secondary antibodies as listed in Supplementary Table 3. Stained sections were imaged using a Leica Aperio Versa automated tissue sectioning scanning microscope (Leica Microsystems, Wetzlar, Germany) equipped with a high-sensitivity monochrome cooling camera (Andor Technology, Zyla, Northern Ireland, UK). Then, the images were analyzed in ImageScope (Leica Biosystems). For each image, we measured the thickness of 4-5 distinct regions and computed the mean value to determine the skin thickness of the sample.

Protein expression and purification

The full-length hTRPV3 gene (NM_001258205.2) was subcloned into a modified pPICZ-B vector containing a PreScission protease cleavage site and a C-terminal GFP-His_{10} tag to facilitate subsequent protein purification. The hTRPV3 channel protein was expressed in *Pichia pastoris*. The *pichia pastoris* were sourced from Professor Deng Zengqing from Wuhan Institute of Virology. After induction, yeast cells were collected by centrifugation, and the resulting cell pellet was resuspended in lysis buffer consisting of in (mM): 50 Tris-HCl (pH 8.0), 150 NaCl, 2 β-mercaptoethanol, 80 imidazole. The suspension was rapidly frozen and stored at −80 °C. In order to purify the TRPV3 protein, the yeast cells were lysed using a high-pressure cell breaker (Union-Biotech) in lysis buffer supplemented with protease inhibitors (phenylmethane sulphonyl fluoride, BBI) and DNase I (Shanghai Yuanye Biotechnology Co. Ltd.). The TRPV3 protein was solubilized in lysis buffer containing 2% (w/v) N-dodecyl-β-d-maltopyranoside (DDM, Anatrace) for 2 h under gentle agitation, followed by centrifugation at 30,000 *g* for 1 h at 4 °C. The clear supernatant was incubated with Ni-NTA resin (GenScript) for 2 h and washed thoroughly with a rinsing buffer containing (in mM) 20 Tris-HCl (pH 8.0), 150 NaCl, 2 β-mercaptoethanol, 100 imidazole, and 0.01% (w/v) glyco-diosgenin (GDN, Anatrace). The TRPV3 protein was ultimately eluted using an elution buffer consisting of (in mM): 20 Tris-HCl (pH 8.0), 150 NaCl, 2 β-mercaptoethanol, 500 imidazole, 0.01% (w/v) GDN.

Reconstitution of TRPV3 channel protein into Nanodiscs

The membrane scaffold protein MSP2N2, used for the reconstitution of TRPV3 nanodiscs, was expressed in Escherichia coli and purified. The eluted MSP2N2 was concentrated to ~7.5 mg/ml, flash-frozen, and stored at −80 °C. The soybean polar lipid extract (Avanti Polar Lipids) dissolved in chloroform was dried under nitrogen gas and subjected to vacuum desiccation for 2 h. Subsequently, the lipids were resuspended in a buffer containing 20 mM Tris-HCl (pH 8.0), 150 mM NaCl, and 14 mM DDM, and sonicated until a clear solution was obtained. The lipid solution was maintained on ice and subjected to sonication immediately prior to nanodisc reconstitution.

For the reconstitution process, the TRPV3 protein, which had been concentrated to approximately 1 mg/ml following elution, was combined with MSP2N2 and soybean lipid in a molar ratio of 1:2:100 (TRPV3 monomer:MSP2N2: lipids). The mixture was incubated for 30 min on ice. Bio-beads SM2 adsorbent (Bio-Rad), equilibrated in 20 mM Tris-HCl (pH 8.0) and 150 mM NaCl buffer, was added to the solution at a final volume of 12.5% (v/v) to initiate nanodisc assembly. The mixture was then gently rotated at 4 °C for 2 h. The solution was then transferred to a new tube, which was then supplemented with an additional batch of bio-beads and homemade PreScission protease, and incubated overnight with gentle rotation. After reconstitution, the bio-beads were removed by pipetting, and the solution was concentrated and subjected to size exclusion chromatography on a Superose 6 10/300 Increase column (Cytiva) that had been pre-equilibrated with SEC buffer (20 mM Tris-HCl pH 8.0, 150 mM NaCl). Subsequently, peak fractions containing the TRPV3-nanodisc complex were collected and further analyzed by SDS-PAGE.

Cryo-electron microscopy sample preparation and data acquisition

For the preparation of $TRPV3_{Apo}$ samples, the TRPV3-nanodisc complex was concentrated to approximately 1.8 mg/ml and prepared for vitrification. For the $TRPV3_{Citronellal}$, $TRPV3_{Linalool}$, $TRPV3_{Isodihydrolavandulal}$, and $TRPV3_{Citral}$ samples, the respective ligand, including citronellal, linalool, isodihydrolavandulal, and citral, was dissolved in SEC buffer, and added to the concentrated TRPV3-nanodisc complex to achieve final concentrations of 10 mM, 12 mM, 10 mM, and 8 mM, respectively. The resulting TRPV3-nanodisc complex concentrations were ~2.0 mg/ml for $TRPV3_{Citronellal}$ and $TRPV3_{Linalool}$ samples, and 2.4 mg/ml for $TRPV3_{Isodihydrolavandulal}$ and $TRPV3_{Citral}$ samples, all supplemented with 1% dimethyl sulfoxide (DMSO). The above mixtures were incubated at ambient temperature for 20–30 min prior to cryo-EM sample preparation. A volume of 3 μL of the incubated TRPV3-nanodisc-drug solutions was applied to glow-discharged grids (Quantifoil Cu R1.2/1.3, 300 mesh). The grids were then blotted for 2–4 s (with a wait time of 5 s and a blotting force of 1) at 4 °C in an environment of 100% humidity, after which they were plunge-frozen in liquid ethane using an FEI Vitrobot Mark IV (Thermo Fisher Scientific). The prepared grids were preserved in liquid nitrogen until data collection began.

Imaging was performed with a Titan Krios microscope (FEI) at an operating voltage of 300 kV, equipped with a K3 Summit direct electron detector (Gatan) and controlled by EPU software. The data were collected in super-resolution mode at magnifications of 81,000×, with a pixel size of 1.07 Å, and 105,000×, with a pixel size of 0.824 Å. The total electron dose of 50 $e^-/Å^2$ was distributed over 32 (81,000× datasets) and 40 (105,000× datasets) frames, respectively. The nominal defocus range was set between −1.4 and −2.4 μm for the 81,000× datasets, and −1.3 and −1.5 μm for the 105,000× datasets. Statistics of cryo-EM data collection were listed in Supplementary Table 4.

Cryo-EM data processing

All data sets were processed in a similar manner using Relion v4.0[56] and cryoSPARC v4.4.1[57]. Dose-fractionated image stacks were subjected to beam-induced motion correction using the MotionCor2 algorithm implemented in cryoSPARC or Relion[58]. Images processed in Relion were then transferred to cryoSPARC for further processing. Contrast transfer function (CTF) estimation was performed using a patch CTF estimation approach, followed by manual curation of exposures to exclude images of poor resolution and quality. Particles were picked using the neural-network-based Topaz picker implemented in cryoSPARC and subjected to several rounds of two-dimensional (2D) classification. An ab-initio 3D reconstruction was performed using the remaining particles, requiring the generation of 3 to 4 classes of volumes, including initial models and garbage collectors. Further refinement was achieved by heterogeneous refinement using the volumes generated in the ab-initio reconstruction as templates, which allowed the exclusion of particles of poor quality. Only the $TRPV3_{Citronellal}$ data processing was performed with binning during the aforementioned process, while all particles from other datasets were directly extracted without binning.

For the $TRPV3_{Apo}$ dataset, the remaining particles were subjected to non-uniform refinement with C4 symmetry imposed, resulting in a construction with an overall resolution of 3.13 Å.

For other ligand-bound TRPV3 datasets, the extracted particles were sorted using 3D classification or 3D variability analysis to effectively reveal structural heterogeneity. In the case of the $TRPV3_{Citronellal}$ dataset, no mask was applied during 3D classification, while in other

datasets, masks covering the vanilloid binding pocket and TRPV3 cytoplasmic N and C termini were applied to perform focused 3D classification or 3D variability analysis. The particles within the best classes, were further subjected to further non-uniform refinement and local refinement with C4 symmetry imposed. The four ligand-bound TRPV3 datasets yielded 3D reconstructions with overall resolutions of 3.53 Å, 3.62 Å, 3.51 Å, and 3.39 Å, respectively. The reported overall resolution for the final maps was estimated in cryoSPARC using the gold-standard Fourier Shell Correlation (FSC) 0.143 criterion. Local resolution was calculated in cryoSPARC using the FSC = 0.5 criterion.

Model building, refinement, and validation

The process of constructing models for $TRPV3_{Apo}$ and $TRPV3_{Citronellal}$ involved a number of steps. The initial models were based on the human wild-type $TRPV3_{Apo}$ (PDB: 6UW4) and human $TRPV3_{K169A\ Apo}$ (PDB: 6UW6). The initial models were then fitted into the cryo-EM density maps using UCSF ChimeraX[59]. Each residue was then meticulously examined and adjusted in COOT[60]. The iterative manual reconstruction process was continued in COOT, followed by real-space refinement in PHENIX[61]. In particular, well-defined lipid-like densities with a one-head-and-two-tails shape were observed in the transmembrane domain. These densities were hypothesized to be TRPV3-bound phospholipids. The lipid densities were then modeled as phosphatidylcholine (PC) lipids. Finally, the model was validated using MolProbity in PHENIX[62]. Statistics of model building, refinement and validation were listed in Supplementary Table 4. In addition, pore radii were calculated for the different models using MOLE-online[63]. All visuals and figures were generated using UCSF ChimeraX.

Statistical analyses

Electrophysiological data were analyzed offline using Qstudio developed by Dr. Feng Qin at the State University of New York at Buffalo, Clampfit (Molecular Devices, Sunnyvale, CA), IGOR (Wavemetrics, Lake Oswego, OR, USA), and OriginPro (Origin Lab Corporation, MA, USA). For concentration-response analysis, the modified Hill equation was used: $Y = A1 + (A2 - A1)/[1 + 10\hat{}\ (\log EC_{50} - X) * n_H]$, where EC_{50} is the half-maximal effective concentration, and n_H is the Hill coefficient. Unless otherwise stated, summary data are presented as mean ± standard error (SEM), from a population of cells (n). Statistical significance was assessed by Student's t-test for two-group comparisons or one-way analysis of variance (ANOVA) followed by Least Significant Difference (LSD) test for multiple group comparisons. Significant difference is indicated by a P value less than 0.05 (*$P < 0.05$, ** $P < 0.01$, *** $P < 0.001$).

Reporting summary

Further information on research design is available in the Nature Portfolio Reporting Summary linked to this article.

Data availability

Plasmids and reagents generated in this study are available on request, and all data reported in this paper are available in a publicly accessible repository. The cryo-EM maps and atomic coordinates of wild-type human TRPV3 in the apo form and ligand-bound states have been deposited in the Electron Microscopy Data Bank and the Protein Data Bank under the accession numbers: EMD-61396, 9JDM for $TRPV3_{Apo}$, EMD-61407, 9JE5 for $TRPV3_{Citronellal}$, EMD-61414, 9JEE for $TRPV3_{Citral}$, EMD-61415, 9JEF for $TRPV3_{Linalool}$, and EMD-61416, 9JEG for $TRPV3_{Isodihydrolavandulal}$. Source data are provided with this paper as a Source Data file. Source data are provided with this paper.

References

1. Wang, W. et al. Neuromorphic sensorimotor loop embodied by monolithically integrated, low-voltage, soft e-skin. *Science* **380**, 735–742 (2023).
2. DeWeerdt, S. PSYCHODERMATOLOGY: an emotional response. *Nature* **492**, 562–563 (2012).
3. Ni, Z. J. et al. Recent updates on the chemistry, bioactivities, mode of action, and industrial applications of plant essential oils. *Trends Food Sci. Technol.* **110**, 78–89 (2021).
4. Paulino, B. N. et al. Beyond natural aromas: the bioactive and technological potential of monoterpenes. *Trends Food Sci. Technol.* **128**, 188–201 (2022).
5. Rahmi, D. et al. Antiaging and skin irritation potential of four main Indonesian essential oils. *Cosmetics* **8** https://doi.org/10.3390/cosmetics8040094 (2021).
6. Dascalu, D., Isvoran, A. & Ianovici, N. Predictions of the biological effects of several acyclic monoterpenes as chemical constituents of essential oils extracted from plants. *Molecules* **28** https://doi.org/10.3390/molecules28124640 (2023).
7. Xu, H. et al. TRPV3 is a calcium-permeable temperature-sensitive cation channel. *Nature* **418**, 181–186 (2002).
8. Peier, A. M. et al. A heat-sensitive TRP channel expressed in keratinocytes. *Science* **296**, 2046–2049 (2002).
9. Smith, G. D. et al. TRPV3 is a temperature-sensitive vanilloid receptor-like protein. *Nature* **418**, 186–190 (2002).
10. Wang, Y. et al. TRPV3 enhances skin keratinocyte proliferation through EGFR-dependent signaling pathways. *Cell Biol. Toxicol.* **37**, 313–330 (2020).
11. Moqrich, A. et al. Impaired thermosensation in mice lacking TRPV3, a heat and camphor sensor in the skin. *Science* **307**, 1468–1472 (2005).
12. Cheng, X. P. et al. TRP CHANNEL REgulates EGFR signaling in hair morphogenesis and skin barrier formation. *Cell* **141**, 331–343 (2010).
13. Aijima, R. et al. The thermosensitive TRPV3 channel contributes to rapid wound healing in oral epithelia. *FASEB J.* **29**, 182–192 (2015).
14. Sahu, R. P. & Goswami, C. Presence of TRPV3 in macrophage lysosomes helps in skin wound healing against bacterial infection. *Exp. Dermatol.* **32**, 60–74 (2022).
15. Wang, Y. J. et al. Scutellarein attenuates atopic dermatitis by selectively inhibiting transient receptor potential vanilloid 3 channels. *Br. J. Pharmacol.* **179**, 4792–4808 (2022).
16. Song, Z. Y. et al. Hair loss caused by gain-of-function mutant is associated with premature differentiation of follicular keratinocytes. *J. Investig. Dermatol.* **141**, 1964–1974 (2021).
17. Duchatelet, S. et al. A new TRPV3 missense mutation in a patient with olmsted syndrome and erythromelalgia. *JAMA Dermatol.* **150**, 303–306 (2014).
18. Zhong, W. et al. Genotype–phenotype correlation of TRPV3-related olmsted syndrome. *J. Investig. Dermatol.* **141**, 545–554 (2021).
19. Guzman, E. & Lucia, A. Essential oils and their individual components in cosmetic products. *Cosmetics* **8** https://doi.org/10.3390/cosmetics8040114 (2021).
20. Park, K. H. et al. The essential role of Ca^{2+} signals in UVB-induced IL-1β secretion in keratinocytes. *J. Investig. Dermatol.* **139**, 1362–1372 (2019).
21. Guo, Y. Y. et al. The transient receptor potential vanilloid 2 (TRPV2) channel facilitates virus infection through the Ca^{2+}-LRMDA axis in myeloid cells. *Adv. Sci.* **9** https://doi.org/10.1002/advs.202202857 (2022).
22. Xiao, R. et al. Calcium plays a central role in the sensitization of TRPV3 channel to repetitive stimulations. *J. Biol. Chem.* **283**, 6162–6174 (2008).
23. Liu, Q. et al. Therapeutic inhibition of keratinocyte TRPV3 sensory channel by local anesthetic dyclonine. *Elife* **10** https://doi.org/10.7554/eLife.68128 (2021).
24. Yao, J., Liu, B. Y. & Qin, F. Modular thermal sensors in temperature-gated transient receptor potential (TRP) channels. *Proc. Natl Acad. Sci. USA* **108**, 11109–11114 (2011).

25. Hu, H. Z. et al. 2-aminoethoxydiphenyl borate is a common activator of TRPV1, TRPV2, and TRPV3. *J. Biol. Chem.* **279**, 35741–35748 (2004).
26. Singh, A. K., McGoldrick, L. L. & Sobolevsky, A. I. Structure and gating mechanism of the transient receptor potential channel TRPV3. *Nat. Struct. Mol. Biol.* **25**, 805–813 (2018).
27. Zubcevic, L. et al. Conformational ensemble of the human TRPV3 ion channel. *Nat. Commun.* **9**, 4773 (2018).
28. Deng, Z. et al. Gating of human TRPV3 in a lipid bilayer. *Nat. Struct. Mol. Biol.* **27**, 635–644 (2020).
29. Shimada, H. et al. The structure of lipid nanodisc-reconstituted TRPV3 reveals the gating mechanism. *Nat. Struct. Mol. Biol.* **27**, 645–652 (2020).
30. Nadezhdin K. D. et al. TRPV3 activation by different agonists accompanied by lipid dissociation from the vanilloid site. *Sci. Adv.* **10** https://doi.org/10.1126/sciadv.adn2453 (2024).
31. Nadezhdin, K. D. et al. Structural mechanism of heat-induced opening of a temperature-sensitive TRP channel. *Nat. Struct. Mol. Biol.* **28**, 564–572 (2021).
32. Zubcevic, L., Borschel, W. F., Hsu, A. L., Borgnia, M. J. & Lee, S. Y. Regulatory switch at the cytoplasmic interface controls TRPV channel gating. *Elife* **8** https://doi.org/10.7554/eLife.47746 (2019).
33. Alves-Silva, J. M. et al. Effect of *Ferulago lutea* (Poir.) Grande essential oil on molecular hallmarks of skin aging. *Plants* **12** https://doi.org/10.3390/plants12213741 (2023).
34. Vaughn, A. R., Clark, A. K., Sivamani, R. K. & Shi, V. Y. Natural oils for skin-barrier repair: ancient compounds now backed by modern science. *Am. J. Clin. Dermatol.* **19**, 103–117 (2017).
35. Vogt-Eisele, A. K. et al. Monoterpenoid agonists of TRPV3. *Br. J. Pharm.* **151**, 530–540 (2007).
36. Xu, H., Delling, M., Jun, J. C. & Clapham, D. E. Oregano, thyme and clove-derived flavors and skin sensitizers activate specific TRP channels. *Nat. Neurosci.* **9**, 628–635 (2006).
37. Naziroglu, M. A novel antagonist of TRPM2 and TRPV4 channels: carvacrol. *Metab. Brain Dis.* **37**, 711–728 (2022).
38. Cui, T. T., Wang, G. X., Wei, N. N. & Wang, K. W. A pivotal role for the activation of TRPV3 channel in itch sensations induced by the natural skin sensitizer carvacrol. *Acta Pharmacol. Sin.* **39**, 331–335 (2018).
39. Tsukazaki, T., Chiang, T. A., Davison, A. F., Attisano, L. & Wrana, J. L. SARA, a FYVE domain protein that recruits Smad2 to the TGFbeta receptor. *Cell* **95**, 779–791 (1998).
40. Um, J. Y. et al. Transient receptor potential vanilloid-3 (TRPV3) channel induces dermal fibrosis via the TRPV3/TSLP/Smad2/3 pathways in dermal fibroblasts. *J. Dermatol. Sci.* **97**, 117–124 (2020).
41. Neuberger, A., Nadezhdin, K. D. & Sobolevsky, A. I. Structural mechanism of TRPV3 channel inhibition by the anesthetic dyclonine. *Nat. Commun.* **13** https://doi.org/10.1038/s41467-022-30537-8 (2022).
42. Neuberger, A., Nadezhdin, K. D., Zakharian, E. & Sobolevsky, A. I. Structural mechanism of TRPV3 channel inhibition by the plant-derived coumarin osthole. *EMBO Rep.* **22**, e53233 (2021).
43. Fan, J. et al. Structural basis of TRPV3 inhibition by an antagonist. *Nat. Chem. Biol.* https://doi.org/10.1038/s41589-022-01166-5 (2022).
44. Nadezhdin, K. D. et al. TRPV3 activation by different agonists accompanied by lipid dissociation from the vanilloid site. *Sci. Adv.* **10** https://doi.org/10.1126/sciadv.adn2453 (2024).
45. Gao, Y., Cao, E., Julius, D. & Cheng, Y. TRPV1 structures in nanodiscs reveal mechanisms of ligand and lipid action. *Nature* **534**, 347–351 (2016).
46. Zhang, K., Julius, D. & Cheng, Y. Structural snapshots of TRPV1 reveal mechanism of polymodal functionality. *Cell* **184**, 5138–5150 e5112 (2021).
47. Arnold, W. R. et al. Structural basis of TRPV1 modulation by endogenous bioactive lipids. *Nat. Struct. Mol. Biol.* https://doi.org/10.1038/s41594-024-01299-2 (2024).
48. Lansky, S. et al. A pentameric TRPV3 channel with a dilated pore. *Nature* https://doi.org/10.1038/s41586-023-06470-1 (2023).
49. Cao, E., Liao, M., Cheng, Y. & Julius, D. TRPV1 structures in distinct conformations reveal activation mechanisms. *Nature* **504**, 113–118 (2013).
50. Yang, F. et al. Structural mechanism underlying capsaicin binding and activation of the TRPV1 ion channel. *Nat. Chem. Biol.* **11**, 518–524 (2015).
51. Kwon, D. H. et al. Heat-dependent opening of TRPV1 in the presence of capsaicin. *Nat. Struct. Mol. Biol.* **28**, 554–563 (2021).
52. Nadezhdin, K. D. et al. Extracellular cap domain is an essential component of the TRPV1 gating mechanism. *Nat. Commun.* **12** https://doi.org/10.1038/s41467-021-22507-3 (2021).
53. Kwon, D. H., Zhang, F., Fedor, J. G., Suo, Y. & Lee, S. Y. Vanilloid-dependent TRPV1 opening trajectory from cryoEM ensemble analysis. *Nat. Commun.* **13**, 2874 (2022).
54. Tian, Q. et al. Identification of an arthropod molecular target for plant-derived natural repellents. *Proc. Natl Acad. Sci. USA* **119**, e2118152119 (2022).
55. Mo, X. Y. et al. The industrial solvent 1,4-dioxane causes hyperalgesia by targeting capsaicin receptor TRPV1. *Bmc Biology* **20** https://doi.org/10.1186/s12915-021-01211-0 (2022).
56. Scheres, S. H. RELION: implementation of a Bayesian approach to cryo-EM structure determination. *J. Struct. Biol.* **180**, 519–530 (2012).
57. Punjani, A., Rubinstein, J. L., Fleet, D. J. & Brubaker, M. A. cryoSPARC: algorithms for rapid unsupervised cryo-EM structure determination. *Nat. Methods* **14**, 290–296 (2017).
58. Zheng, S. Q. et al. MotionCor2: anisotropic correction of beam-induced motion for improved cryo-electron microscopy. *Nat. Methods* **14**, 331–332 (2017).
59. Pettersen, E. F. et al. UCSF ChimeraX: structure visualization for researchers, educators, and developers. *Protein Sci.* **30**, 70–82 (2021).
60. Emsley, P., Lohkamp, B., Scott, W. G. & Cowtan, K. Features and development of Coot. *Acta Crystallogr D. Biol. Crystallogr* **66**, 486–501 (2010).
61. Adams, P. D. et al. PHENIX: a comprehensive Python-based system for macromolecular structure solution. *Acta Crystallogr D. Biol. Crystallogr* **66**, 213–221 (2010).
62. Chen, V. B. et al. *MolProbity*: all-atom structure validation for macromolecular crystallography. *Acta Crystallogr. Sect. D. Biol. Crystallogr.* **66**, 12–21 (2010).
63. Petrek, M., Kosinova, P., Koca, J. & Otyepka, M. MOLE: a Voronoi diagram-based explorer of molecular channels, pores, and tunnels. *Structure* **15**, 1357–1363 (2007).

Acknowledgements

We are grateful to our colleagues and members of Yao lab for their insightful comments and valuable discussions to this study. Single-particle cryo-EM data were collected at the Cryo-EM Center of the University of Science and Technology of China and the Cryo-EM Platform of Wuhan University. We gratefully acknowledge the invaluable assistance provided by senior experimenters Danyang Li, Xiangning Li and Yongxiang Gao in the process of cryo-electron microscopy data acquisition and analysis. We thank Dr. Xinlian Liu from the Core Facility of State Key Laboratory of Hybrid Rice of Wuhan University for her assistance with AKTA pure FPLC system. We sincerely thank Professor Xiangrong Liu of Xiamen University for his constructive suggestions. We also would like to thank the core facilities of the College of Life Sciences at Wuhan University for technical help. This work was supported by grants from the National Key Research and Development Program of China (2023YFF1204000 to J.Y., 2024YFA1306500 to J.Y.), National Natural Science Foundation of China (32171147 to J.Y., 32371200 to J.Y., and 32370761 to C.X.), and the Fundamental Research Funds for the Central Universities (2042022dx0003 to J.Y.).

Author contributions

J.Y. designed and supervised the study. Y.L., X.L., X.C., K.X., J.H., P.W., P.P., B.G., D.S., Z.Z., D.L., Z.D., C.T., C.X., and J.Y. carried out the experiments and analyzed data. Y.L., X.L., and J.Y. wrote the paper with inputs from all other authors. All authors read and approved the final manuscript.

Competing interests

The authors declare no competing interests.

Additional information

Supplementary information The online version contains supplementary material available at https://doi.org/10.1038/s41467-025-58033-9.

Correspondence and requests for materials should be addressed to Jing Yao.

Peer review information *Nature Communications* thanks Yifan Cheng, Mingliang Jin and Makoto Tominaga for their contribution to the peer review of this work. A peer review file is available.

Reprints and permissions information is available at http://www.nature.com/reprints

Publisher's note Springer Nature remains neutral with regard to jurisdictional claims in published maps and institutional affiliations.

Open Access This article is licensed under a Creative Commons Attribution-NonCommercial-NoDerivatives 4.0 International License, which permits any non-commercial use, sharing, distribution and reproduction in any medium or format, as long as you give appropriate credit to the original author(s) and the source, provide a link to the Creative Commons licence, and indicate if you modified the licensed material. You do not have permission under this licence to share adapted material derived from this article or parts of it. The images or other third party material in this article are included in the article's Creative Commons licence, unless indicated otherwise in a credit line to the material. If material is not included in the article's Creative Commons licence and your intended use is not permitted by statutory regulation or exceeds the permitted use, you will need to obtain permission directly from the copyright holder. To view a copy of this licence, visit http://creativecommons.org/licenses/by-nc-nd/4.0/.

© The Author(s) 2025